Vita Summary

1 Name and Surename

Name: Paweł Tecmer

2 Education

2008–2012	Ph.D. Faculty of Exact Sciences, Vrije University Amsterdam, Amsterdam, The Netherlands; title of thesis: *Towards reliable modeling of excited states of uranium compounds*; supervisor: Prof. Lucas Visscher; date of defence: 02.10.2012
2006–2008	M.Sc. General Chemistry, Faculty of Chemistry, Nicolaus Copernicus University in Torun, Poland; title of thesis: *Atomic basis sets for closed-shell atoms in the two-component IOTC method*; supervisor: Prof. Maria Barysz; date of defence: 20.05.2008
2003–2006	B.Sc. Chemistry with Applied Informatics, Faculty of Chemistry, Nicolaus Copernicus University in Torun, Poland; date of defence: 30.06.2006

3 Employment

03/2017–present	Assistant Professor, Faculty of Physics, Astronomy and Informatics, Nicolaus Copernicus University in Torun, Poland
04/2016–02/2017	Research Assistant, Faculty of Physics, Astronomy and Informatics, Nicolaus Copernicus University in Torun, Poland
01/2016–03/2016	Researcher/Visiting Professor, Faculty of Physics, Astronomy, and Applied Informatics, Nicolaus Copernicus University in Torun, Poland

Paweł Tecmer

07/2013–12/2015	Postdoctoral Fellow, Department of Chemistry and Chemical Biology, McMaster University, Hamilton, Canada
07/2012–06/2013	Postdoctoral Fellow, Laboratory of Physical Chemistry, ETH Zurich, Switzerland

4 Scientific achievements

(a) Title of scientific achievement

Series of publications:
"Accurate and inexpensive treatment of electron correlation effects using conventional and unconventional electronic structure methods with application focus on heavy element chemistry"

(b) Authors, titles, year of publication, name of the journal

Additional information on the contributions of all authors are given in separate Appendices, including statements of the other coauthors.

[H1] **P. Tecmer** and C. E. González–Espinoza *"Electron correlation effects of the ThO and ThS molecules in the spinor basis. A relativistic coupled cluster study of ground and excited states properties"*, *Phys. Chem. Chem. Phys.* 20 **2018**, 23424–23432 (**corresponding author**).
My estimated contribution to the paper: 95%

[H2] K. Boguslawski, F. Réal, **P. Tecmer**, C. Duperrouzel, A. S. P. Gomes, Ö. Legeza, P. W. Ayers, and V. Vallet *"On the multi-reference nature of plutonium oxides: PuO_2^{2+}, PuO_2, PuO_3, and $PuO_2(OH)_2$"*, *Phys. Chem. Chem. Phys.* 19 **2017**, 4317–4329.
My estimated contribution to the paper: 20%

[H3] **P. Tecmer**, S. W. Hong, and K. Boguslawski *"Dissecting the Cation-Cation Interaction between Two Uranyl Units"*, *Phys. Chem. Chem. Phys.* 18 **2016**, 18305–18311 (**corresponding author**).
My estimated contribution to the paper: 80%

[H4] **P. Tecmer**, K. Boguslawski, and P. W. Ayers *"Singlet Ground State Actinide Chemistry with Geminals"*, *Phys. Chem. Chem. Phys.* 17 **2015**, 14427–14436 .
My estimated contribution to the paper: 90%

[H5] C. Duperrouzel, **P. Tecmer**, K. Boguslawski, G. Barcza, Ö. Legeza, and P. W. Ayers *"A Quantum Informational Approach for Dissecting Chemical Reactions"*, *Chem. Phys. Lett.* 621 **2015**, 160–164 (**corresponding author**).
My estimated contribution to the paper: 40%

[H6] **P. Tecmer**, A. S. P. Gomes, S. Knecht, and L. Visscher *"Communication: Relativistic Fock-Space Coupled Cluster Study of Small Building Blocks of Larger*

Paweł Tecmer

Uranium Complexes", *J. Chem. Phys.* 141 **2014**, 041107 (**corresponding author**).
My estimated contribution to the paper: 90%

[H7] M. Mottet, **P. Tecmer**, K. Boguslawski, Ö. Legeza, and M. Reiher *"Quantum Entanglement in Carbon-Carbon, Carbon-Phosphorus, and Silicon-Silicon Bonds"*, *Phys. Chem. Chem. Phys.* 16 **2014**, 8872–8880 (**corresponding author**).
My estimated contribution to the paper: 30%

[H8] **P. Tecmer**, K. Boguslawski, Ö. Legeza, and M. Reiher *"Unravelling the Quantum-Entanglement Effect of Noble Gas Coordination on the spin Ground State of CUO"*, *Phys. Chem. Chem. Phys.* 16 **2014**, 719–727 (**corresponding author**).
My estimated contribution to the paper: 80%

[H9] K. Boguslawski, **P. Tecmer**, G. Barcza, Ö. Legeza, and M. Reiher *"Orbital Entanglement in Bond-Formation Processes"*, *J. Chem. Theory Comput.* 9 **2013**, 2959–2973.
My estimated contribution to the paper: 30%

[H10] K. Boguslawski, **P. Tecmer**, Ö. Legeza, and M. Reiher *"Entanglement Measures for Single- and Multi-reference Correlation Effects"*, *J. Phys. Chem. Lett.* 3 **2012**, 3129–3135.
My estimated contribution to the paper: 40%

(c) Discussion of scientific goals, obtained results, and their significance

c.1 Introduction and motivation

A detailed understanding of the smallest building blocks of matter, that is, atoms and molecules, is of crucial importance in many areas of physics, chemistry, biology, and materials sciences. One way to achieve this goal is to use the quantum mechanical description of their electronic structures in which the correlated motion of electrons is taken into account. The exact solution of the electronic Schrödinger equation[1] and inclusion of all types of electron correlation effects in a given basis set (working within the Born–Oppenheimer approximation[2]) can be obtained from the full configuration interaction (FCI) approach. This approach is, however, limited to small model systems as it scales factorially with the number of electrons and basis functions. To model larger, more realistic molecules and clusters, a number of approximate electron correlation methods have been developed. In general, these approximate methods can be divided into two categories, one that is based on the density as the main constituent, the so-called density functional theory approach, and the other one that optimizes an approximate N-electron wave function. Furthermore, to be applicable to heavy element chemistry, that is, atoms and molecules with large atomic numbers, we have to build in relativistic effects in the electronic Schrödinger

Paweł Tecmer

equation, which brings additional computational difficulties on top of electron correlation. Thus, the main goal of current developments of electronic structure methods is to find a computationally feasible model to account for both electron correlation and relativistic effects, which still provides reliable results.

c.2 Relativistic effects

The most rigorous theoretical treatment of relativistic effects in atoms, molecules, and clusters comes form Dirac's relativistic quantum mechanics,[3–5] namely the Dirac equation in which the Hamiltonian and the wave function have four-component forms,

$$\begin{pmatrix} \hat{V}\hat{\boldsymbol{I}}_2 & c\hat{\boldsymbol{\sigma}}\cdot\hat{\boldsymbol{p}} \\ c\hat{\boldsymbol{\sigma}}\cdot\hat{\boldsymbol{p}} & (\hat{V}-2c^2)\hat{\boldsymbol{I}}_2 \end{pmatrix} \begin{pmatrix} \psi^L(\boldsymbol{r}) \\ \psi^S(\boldsymbol{r}) \end{pmatrix} = \epsilon \begin{pmatrix} \psi^L(\boldsymbol{r}) \\ \psi^S(\boldsymbol{r}) \end{pmatrix}. \tag{1}$$

In the above equation c indicates the velocity of light, $\hat{\boldsymbol{p}} = (\hat{p}_x, \hat{p}_y, \hat{p}_z)$ is the momentum operator, and $\hat{V}$ is the Coulomb potential (electron-nuclear interaction), $\epsilon = E - c^2$ is the adjusted (scaled) Dirac energy, and

$$\hat{\boldsymbol{\alpha}}_i = \begin{pmatrix} 0 & \hat{\boldsymbol{\sigma}}_i \\ \hat{\boldsymbol{\sigma}}_i & 0 \end{pmatrix}, \quad \hat{\boldsymbol{\beta}} = \begin{pmatrix} \hat{\boldsymbol{I}}_2 & 0 \\ 0 & -\hat{\boldsymbol{I}}_2 \end{pmatrix}, \tag{2}$$

with $\hat{\boldsymbol{I}}_2$ being the two-dimensional unity matrices and $\boldsymbol{\sigma}_i$ the (two-dimensional) Pauli spin matrices

$$\hat{\boldsymbol{\sigma}}_x = \begin{pmatrix} 0 & 1 \\ 1 & 0 \end{pmatrix}, \quad \hat{\boldsymbol{\sigma}}_y = \begin{pmatrix} 0 & -i \\ i & 0 \end{pmatrix}, \quad \hat{\boldsymbol{\sigma}}_z = \begin{pmatrix} 1 & 0 \\ 0 & -1 \end{pmatrix}. \tag{3}$$

The two-component wave functions are called the large $\psi^L(\boldsymbol{r})$ and small $\psi^S(\boldsymbol{r})$ component, respectively. This naming convention comes from the fact that, for the electronic solutions, the large component has a larger norm than the small component.[6–8] The Dirac equation, describes thus the behavior of both electrons and positrons, and naturally accounts for spin via the $\hat{\boldsymbol{\sigma}}$ matrices. One should note that in non-relativistic quantum mechanics, the existence of the electron spin is postulated and included only *a posteriori* into the model. In the four-component Dirac formalism, scalar relativistic and magnetic effects (such as spin–orbit and spin–other–orbit interactions) are intertwined and consistently included.

The starting point in relativistic quantum chemistry is the four-component Dirac–Coulomb–Breit Hamiltonian (in the Born–Oppenheimer approximation),

$$\hat{H}^{\mathrm{DCB}} = \sum_A \sum_i \left[c\left(\hat{\boldsymbol{\alpha}}\cdot\hat{\boldsymbol{p}}\right)_i + \hat{\boldsymbol{\beta}}_i c^2 + \hat{V}_{iA} \right] + \sum_{i<j} \left[\frac{1}{|\mathbf{r}_i - \mathbf{r}_j|} + \hat{O}(i,j)^{\mathrm{Breit}} \right] + \sum_{A<B} \hat{V}_{AB}, \tag{4}$$

where A and B denotes nuclei and i and j electrons, respectively, $\hat{V}_{iA}$ is the nuclear-electron attraction term, $\frac{1}{|\mathbf{r}_i - \mathbf{r}_j|}$ is the Coulomb term, $\hat{V}_{AB}$ is the standard nuclear

Paweł Tecmer

attraction term, and

$$\hat{O}(i,j)^{\text{Breit}} = -\frac{c\hat{\boldsymbol{\alpha}}_i \cdot c\hat{\boldsymbol{\alpha}}_j}{2c^2 r_{ij}} - \frac{(c\hat{\boldsymbol{\alpha}}_i \mathbf{r}_{ij}) \cdot (c\hat{\boldsymbol{\alpha}}_j \mathbf{r}_{ij})}{2c^2 r_{ij}^3}. \tag{5}$$

In addition to the charge–charge interaction present in the Coulomb term, the Breit operator also accounts for the current–current interaction.[9] In practical applications of the four-component methodology, the two-electron part of the Dirac–Coulomb–Breit Hamiltonian is, however, further approximated. A common approach is to keep only the first term in eq. (5), which leads to the so-called Dirac–Coulomb–Gaunt Hamiltonian. However, in most of the four-component applications, the Breit term is completely discarded, which results in the so-called Dirac–Coulomb relativistic Hamiltonian.

Even more popular and computational more favorable approaches take into account only the scalar relativistic effects.[10], either using an effective core potential[11] or employing a two-component strategy[12–15] In the first case the inner core electronic structure is modelled with a relativistic potential that mimics the contraction of s and p inner shells and the valence electrons are treated explicitly such that their energy levels are close to the original (spin–free) Dirac–Coulomb Hamiltonian. In the second approach all electrons are accounted for after modification of the one-electron part of the Schrödinger Hamiltonian such that it resembles the spin–free Dirac–Coulomb energy levels.[15] The advantage of scalar relativistic Hamiltonians is their simple one-component form, which can be easy implemented in standard (one-component) electronic structure codes. If necessary, spin–orbit interaction can be added *a posteriori* on top of a scalar relativistic Hamiltonian.[7]

c.3 Electron correlation effects and molecular properties

Electron correlation effects usually account for about 1% of the total electronic energy of the (molecular) system. However, they are crucial for an accurate and reliable description of the electronic structure of atoms, molecules, and clusters as well as their properties. Qualitatively speaking, electron correlation effects are electronic interactions[16] beyond the mean-field approach. Even though an exact separation of the correlation energy into individual contributions is not possible, one usually divides correlation effects into three different categories, which are denoted dynamic, static, and nondynamic. Although unique definitions of nondynamic, static, and dynamic electron correlation do not exist, the dynamic part is considered to be responsible for keeping electrons apart and is attributed to a large number of configurations, i.e., Slater determinants or configuration state functions, with small (absolute) coefficients in the wave function expansion, while the nondynamic and static contributions involve only some determinants with large (absolute) weights, which are necessary for an appropriate treatment of the quasi-degeneracy of orbitals.[17–19] In particular, static electron correlation embraces a suitable combination of determinants to account for proper spin symmetries and their interactions, whereas nondynamic correlation is required to allow a molecule to separate correctly into its fragments.[18,19] An accurate treatment of dynamic, nondynamic, and static electron correlation effects is covered by the FCI solution.[20]

Paweł Tecmer

c.3.1 Assessment of electron correlation effects

In order to study larger, more realistic and more interesting systems, the FCI wave function needs to be approximated using either single-reference or multi-reference quantum chemical methods. While single-reference approaches like, for instance, Møller–Plesset perturbation theory or the coupled cluster (CC) ansatz, are able to capture a large fraction of the dynamic correlation energy,[19] the missing nondynamic and static contributions can be recovered by usually more expensive multi-reference methods.[21,22] Thus, employing any wave-function based electron correlation approach requires some *a priori* knowledge about the interplay of dynamic, nondynamic, and static electron correlation effects. The proper choice of the quantum chemistry method is indispensable for obtaining reliable results.
Up to date, a number of different diagnostic tools have been developed to characterize the single- or multi-reference nature of molecular systems in order to validate the quality and performance of single-reference quantum chemical methods. For instance, if the absolute or squared weight of the reference configuration (the $|C_0|$ coefficient) obtained from a CI calculation are above a certain threshold ($|C_0| > 0.95$ or $C_0^2 > 0.90$), the electronic structure is considered to be of single-reference nature.[23] However, the weight of the principal configuration can only be considered reliable if, for instance, a complete-active-space self-consistent-field (CASSCF) calculation is feasible and comprises all critical orbitals in the active space. As an alternative measure, Lee *at al.*[23–25] proposed to analyze the Euclidean norm of the t_1 amplitudes optimized in a CC calculation, which is usually denoted as T_1 diagnostics. It was shown that single-reference CC can be considered accurate when the T_1 diagnostic is smaller than 0.02 for main group elements[23,24,26] and 0.05 for transition metals[27] and actinide compounds,[28,29] respectively.

c.3.2 A new look into electron correlation effects

Since electron correlation effects are caused by the interaction of electrons that occupy specific orbitals used to construct the Slater determinant basis, an intuitive way to study electron correlation would be to measure the interaction among any pair of orbitals or the interaction of one orbital with the remaining ones which are incorporated in a FCI wave function. The interaction between orbitals or electrons can be calculated employing concepts from quantum information theory like the von Neumann entropy or the mutual information.[30] So far, such correlation measures have been evaluated employing the one-particle reduced density matrix in terms of natural occupation numbers,[31] the two-particle reduced density matrix or its cumulant in terms of their Frobenius norm,[32–35] and the weights from excited configurations of some wave function expansion.
In **[H10]**, a different way of quantifying electron correlation effects has been proposed. In contrast to the approaches mentioned above, the proposed electron correlation measure is based on many-particle reduced density matrices whose eigenvalue spectra are employed to classify the entanglement of orbitals. Following earlier work on the development of the Density Matrix Renormalization Group (DMRG)[36–38] algorithm

Paweł Tecmer

and orbital ordering,[39,40] we can define the single-orbital entropy,

$$s(1)_i = -\sum_{\alpha=1}^{4} \omega_{\alpha,i} \ln \omega_{\alpha,i}, \tag{6}$$

from the eigenvalues $\omega_{\alpha,i}$ of the one-orbital reduced density matrix (RDM) of orbital i. Such a one-orbital RDM is determined from an N-particle RDM by tracing out all other orbital-degrees of freedom except those of orbital i and therefore its dimension is equal to the dimension of the one-orbital Fock space. In the case of spatial orbitals, four different states (occupations of orbitals) exist, which can be empty $|{-}\rangle$, occupied with an α-(spin-up) $|{\uparrow}\rangle$ or a β-(spin-down) $|{\downarrow}\rangle$ electron, or doubly occupied with two electrons of paired spin $|{\updownarrow}\rangle$.
Furthermore, if the Hilbert space is divided into a subspace spanned by two orbitals and the space spanned by the remaining $k-2$ orbitals, the entanglement entropy quantifies the interaction between one orbital pair and the orbital bath. This two-orbital entropy $s(2)_{i,j}$ is determined from two-orbital RDM with the basis states of a two-orbital Fock space (with 16 possible states for spatial orbitals: $|{-}{-}\rangle$, $|{-}{\downarrow}\rangle$, $|{\downarrow}{-}\rangle$, $|{-}{\uparrow}\rangle$, ..., $|{\updownarrow}{\updownarrow}\rangle$). Thus, the two-orbital analogue of Eq (6) is

$$s(2)_{i,j} = -\sum_{\alpha=1}^{16} \omega_{\alpha,i,j} \ln \omega_{\alpha,i,j}, \tag{7}$$

where $\omega_{\alpha,i,j}$ are the eigenvalues of the two-orbital RDM.
The total amount of correlation between any pair of orbitals (i,j) can be evaluated from the (orbital-pair) mutual information. Specifically, the mutual information allows us to measure the total amount of information one system (here, orbital i) has about another system (here, orbital j), including all types of correlation (classic and quantum).[41–43] According to Rissler *et al.*,[39] the orbital-pair mutual information is calculated using the single- and two-orbital entropy and thus requires the one- and two-orbital RDMs,

$$I_{i|j} = \frac{1}{2}\big(s(2)_{i,j} - s(1)_i - s(1)_j\big)\big(1-\delta_{ij}\big), \tag{8}$$

where δ_{ij} is the Kronecker delta. One should note that a correlated wave function is required to have non-zero orbital entanglement and correlation. Otherwise, the (orbital) entanglement entropy is simply zero.[39]
It has been demonstrated in **[H10]** that a quantitative measure to assess electron correlation effects that are independent of the reference wave function and do not require an *a priori* knowledge about the single- or multi-reference character of the electronic structure can be obtained from the single orbital entropy and mutual information calculated within the DMRG algorithm. The static, nondynamic, and dynamic contributions to the correlation energy can be distinguished by examining the entanglement patterns of orbitals. Specifically, it has been shown for the iron nitrosyl complex ($Fe(NO)^{2+}$), a well-known multi-reference system, that the multi-reference nature of electronic structure is encoded in the mutual information and single orbital

Paweł Tecmer

entropies. These quantities do not significantly depend on the accuracy of the DMRG calculations and can be already obtained from fast and inexpensive DMRG sweeps. The cost for these DMRG sweeps needed to acquire the entanglement measures is thus negligible.

Obtaining many-particle reduced density matrices for entanglement measures.
The DMRG algorithm[44–46] represents an efficient approach to systematically approximate the FCI solution for large molecules and complicated electronic structures and therefore allows us to treat large active orbital spaces without a predefined truncation of the complete N-particle Hilbert space. In particular, DMRG can be considered as a CASCI method whose wave function is constructed from many-particle basis states that are determined from the eigenvalue spectrum of the many-particle reduced density matrix of the system under study. These many-particle basis states are optimized iteratively in one sweep of the DMRG algorithm (in order to obtain a converged energy, several of such sweeps are necessary). Thus the eigenvalues of the many-particle reduced density matrix that will enter the diagnostic analysis proposed in **[H10]** can be easily determined from the DMRG wave function at the end of one DMRG sweep. The calculation of the one- and two-orbital reduced density matrices from generalized correlation functions of the DMRG algorithm whose eigenvalues enter the single-orbital entropy and mutual information has been discussed in **[H9]**. Alternatively, the single orbital entropy (6) and mutual information (8) can be calculated from standard many-particle reduced density matrices of any other electron correlated method. Since, however, calculating elements of higher order reduced density matrices of correlated wave functions is expensive, this approach is rather impractical. One exception is the AP1roG (Antisymmetric Product of 1-reference orbital Geminal) also known as pair coupled cluster doubles. Combined with a variational orbital optimization protocol and denoted as the voo-AP1roG model, represents an inexpensive and reliable approach to model strongly correlated electrons in closed shell systems. Its simple form allows us to efficiently evaluate the single orbital entropy and mutual information using only elements of 1- and 2-reduced density matrices.[47,48] Specifically, the AP1roG ansatz can be written as

$$|\mathrm{AP1roG}\rangle = \exp\left(\sum_{i=1}^{P}\sum_{a=P+1}^{K} c_i^a a_a^\dagger a_{\bar{a}}^\dagger a_{\bar{i}} a_i\right)|\Phi_0\rangle, \tag{9}$$

where a_p, $a_{\bar{p}}$ are the electron annihilation operators for spin-up (p) and spin-down electrons ($\bar{p}$), $|\Phi_0\rangle$ is some independent-particle wave function (for instance the Hartree–Fock (HF) determinant), and $\{c_i^a\}$ is the geminal coefficient matrix. Similar to orbital optimized coupled cluster methods, there are different techniques to optimize the one-particle basis functions within the AP1roG framework[49–51]. Recent numerical studies showed that the variational orbital optimization (vOO-AP1roG[49]) approach is superior to approximate non-variational techniques and represents the most robust and reliable orbital optimization scheme for AP1roG[50,51]. In this optimization scheme, the orbitals are chosen to minimize the AP1roG energy functional subject to the constraint that the AP1roG coefficient equations are satisfied. In

Paweł Tecmer

intermediate normalization, the energy Lagrangian has the form

$$\mathcal{L} = \langle \Phi_0 | e^{\boldsymbol{\kappa}} \hat{H} e^{-\boldsymbol{\kappa}} | \mathrm{AP1roG} \rangle + \sum_{i,a} \lambda_i^a \left(\langle \Phi_{i\bar{i}}^{a\bar{a}} | e^{\boldsymbol{\kappa}} \hat{H} e^{-\boldsymbol{\kappa}} | \mathrm{AP1roG} \rangle - E c_i^a \right), \tag{10}$$

where $\{\lambda_i^a\}$ are the Lagrange multipliers and κ denotes the orbital rotation. The requirement that the derivative of $\mathcal{L}$ with respect to the Lagrange multipliers $\{\lambda_i^a\}$ is stationary results in the standard set of equations for the geminal coefficients $\{c_i^a\}$[49], while the stationary requirement of $\mathcal{L}$ with respect to the geminal coefficients, $\frac{\partial \mathcal{L}}{\partial c_i^a} = 0$, leads to a set of equations for the Lagrange multipliers, analogous to the Λ-equations in CC theory.[20] Finally, the variational orbital gradient is the derivative of $\mathcal{L}$ with respect to the orbital rotation coefficients $\{\kappa_{pq}\}$.[51]

c.3.3 An alternative approach to dissect orbital interactions and chemical bonds

The findings reported in **[H10]** motivated more elaborate studies of electron correlation effects for a series of both known and unknown molecular electronic structures. Specifically, in **[H9]**, a series of diatomic molecules with well-known multi-reference character such as N_2, F_2, and CsH have been investigated along their potential energy surface. In addition, in **[H9]**, it has been shown that entanglement-based measures can be instrumental for an analysis of bond-breaking and bond-forming processes. It is important to understand that these measures allow us to extract orbital-related information from a correlated wave function. The single-orbital entropies and mutual information corresponding to the molecular orbitals forming a chemical bond show large values when bonds are stretched. All other orbitals remain slightly entangled with small values for $s(1)_i$ and $I_{i,j}$. Such patterns are consistent with the understanding of nondynamic correlation effects, where those orbitals become strongly entangled, which allow a molecule to correctly separate into its fragments. The one- and two-orbital entanglement measures should, therefore, provide a qualitative picture of how many bonds are formed between two atoms. A qualitative, entanglement-based bond order can be determined from the total number of steep changes in the $s(1)_i$-diagram present in the dissociation limit (divided by two to account for the bonding and anti-bonding combination of molecular orbitals), which will be demonstrated in the following sections.

Furthermore, the process of bond-breaking or bond-forming along a reaction coordinate can be monitored in the evolution of the single-orbital entropies. Since static and nondynamic electron correlation effects become dominant if bonds are stretched, the single-orbital entropies corresponding to the bonding and anti-bonding pair of molecular orbitals should increase gradually. In particular, the rate of growth should depend on the type (or strength) of a specific bond as the magnitude of the one- and two-orbital entanglement measures is connected to the structure of the electronic wave function. In a qualitative picture, the $s(1)_i$ values of orbitals involved in weak π-bonds increase faster than those corresponding to strong σ-bonds. A chemical bond is considered broken if the $s(1)_i$ remain unchanged when the two centers A and B

Paweł Tecmer

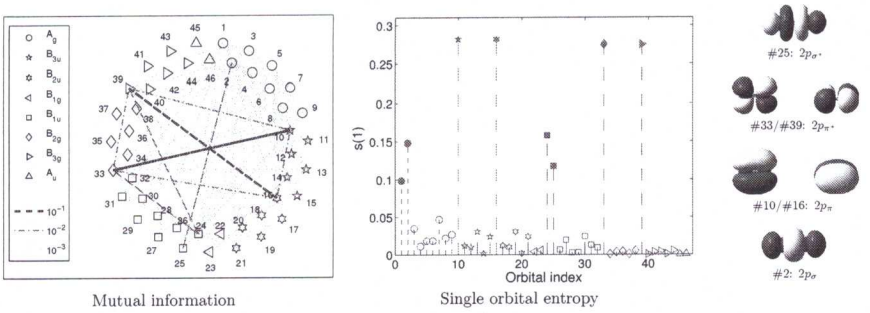

Mutual information Single orbital entropy

(a) $d_{\mathrm{NN}} = 1.12$Å

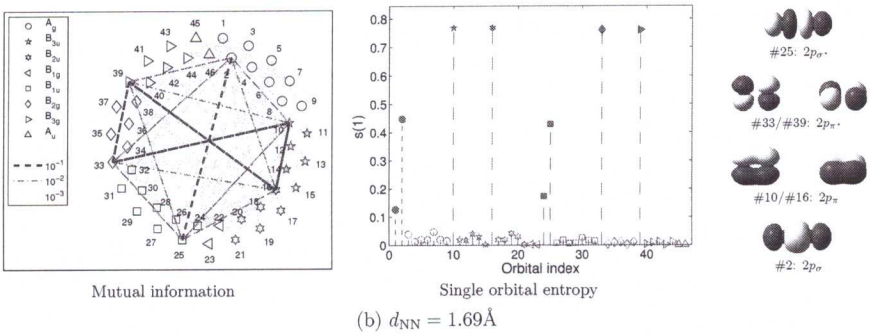

Mutual information Single orbital entropy

(b) $d_{\mathrm{NN}} = 1.69$Å

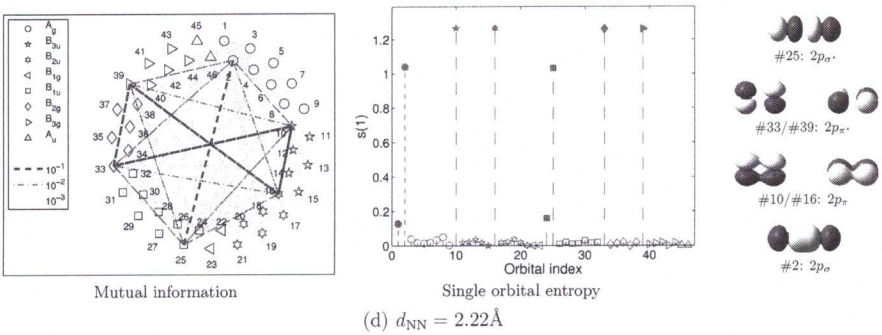

Mutual information Single orbital entropy

(d) $d_{\mathrm{NN}} = 2.22$Å

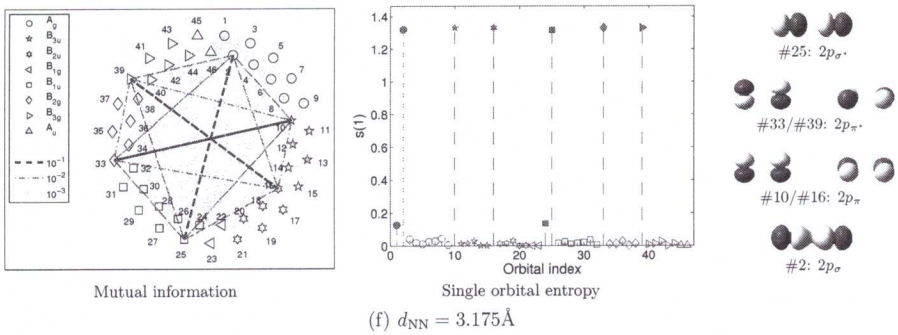

Mutual information Single orbital entropy

(f) $d_{\mathrm{NN}} = 3.175$Å

Figure 1: Mutual information and single-orbital entropies $s(1)_i$ from DMRG(10,46)[512,1024,10^{-5}] calculations for the N_2 molecule at different internuclear distances. Each orbital index in the $s(1)_i$ diagram (middle; those included in the CAS(10,8)SCF calculations are marked in red) corresponds to the same natural orbital as numbered in the entanglement plot (left).

Paweł Tecmer

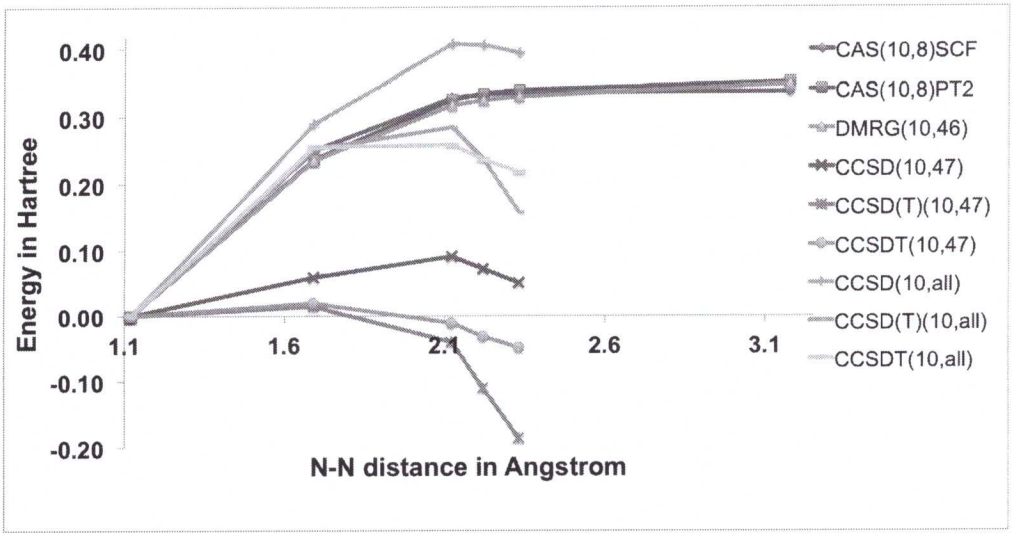

Figure 2: Electronic energy differences for the N_2 molecule at various intermolecular distances determined by different quantum chemical methods. The energy reference is the electronic energy at equilibrium distance of each method.

are further pulled apart, i.e., if $\partial s(1)_i/\partial r_{AB} \to 0$, and thus $\partial I_{\text{tot}}/\partial r_{AB} \to 0$ for large bond lengths r_{AB}. This should allow us to resolve bond-breaking processes of individual σ-, π-, or δ-bonds in multi-bonded centers.

Dissociation of N_2. Around the equilibrium distance the N_2 molecule has a single reference nature and can be well represented by single reference methods such as standard coupled cluster approaches. As shown in Figure 1, in this region, both π- and π^*-orbitals (#10-#33,#16-#39) are strongly entangled, followed by the bonding and anti-bonding combinations of the σ-orbitals (#2-#25), while all remaining orbitals are important to capture dynamic electron correlation effects. When the nitrogen atoms are pulled apart, the single-orbital entropies corresponding to the σ, σ^*, π, and π^*-orbitals increase considerably. However, we still observe a large number of orbitals that are dynamically entangled. This explains the qualitatively good performance of the CCSD(T)(14,all) and CCSDT(14,all) calculations close to the equilibrium structure and for small internuclear distances compared to the DMRG reference (see Figure 2). However, the amount of dynamic correlation decreases upon dissociation, and the system becomes dominated by static and nondynamic electron correlation. In the case of the N_2 molecule, we should be able to distinguish the dissociation of two π-bonds and one σ-bond. If the N atoms are pulled apart, the single-orbital entropies corresponding to the π- and π^*-orbital pairs increase considerably faster than those corresponding to the bonding and anti-bonding combination of σ-orbitals. Thus, the weaker π-bonds are breaking first under dissociation, followed by the stronger σ-bond. If the nitrogen atoms are pulled further apart, from a distance of approximately 1.6 Å onward, the σ-bond gets weakened and the corresponding single-orbital entropies increase most extensively, while the $s(1)_i$ values associated with the π-bonds grow more slowly. In the dissociation limit, where both the σ- and π-bonds are broken, the

Paweł Tecmer

single-orbital entropies corresponding to the bonding and anti-bonding combination reach their maximum value of ln 4, first observed for the weaker π-bonds, followed by the stronger σ-bond.

Monitoring bond breaking processes in larger molecules. In a follow up work (**[H7]**), our test set has been extended to larger molecular systems covering C_2, $[CP]^-$, HCP, C_2H_2, C_2H_4, C_2H_6, Si_2H_2, and Si_2H_4. As an example, the hydrocarbon series will be discussed in details. It is well-known and generally accepted that the carbon–carbon bond is weakest in alkanes, stronger in alkenes, and strongest in alkynes, where singly-, doubly- and triply-bonded centers are formed, respectively. In this study, we choose the three lightest carbon-containing representatives of the hydrocarbon series ethane (C_2H_6), ethene (C_2H_4), and acetylene (C_2H_2). These molecules represent a prototypical test set to study the bond multiplicities in polyatomic molecules by means of quantum entanglement.
Figure 3 shows the mutual information and single-orbital entropies obtained from DMRG(14,28) calculations for the C_2H_6 molecule at two different carbon–carbon distances: $1.0r_e$ and $2.0r_e$. At the inter-nuclear distance of $1.0r_e$, all orbitals are moderately and weakly entangled and it remains rather difficult to identify the bonding and anti-bonding combinations of molecular orbitals corresponding to the single-bond of interest. When the H_3C fragments are pulled apart, a gradual increase in mutual information and single-orbital entropies can be observed for the bonding and anti-bonding p_σ-orbitals (#3 and #17) in Figure 3 reaching the value of about 0.7 in the vicinity of dissociation. Our entanglement analysis correctly predicts a bond order of 1 between the two carbon centers of C_2H_6 (cf. Figure 3).

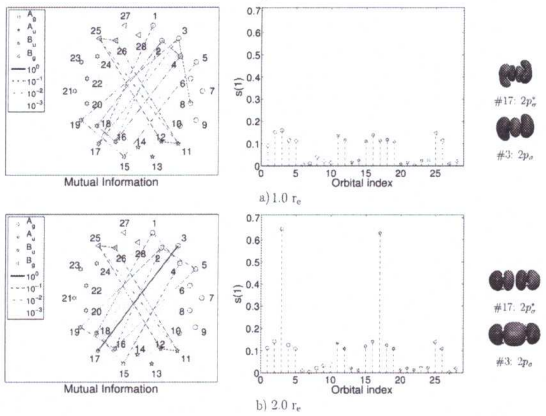

Figure 3: Mutual information and single orbital entropies $s(1)_i$ for DMRG(14,28)$[1024, 512, 10^{-5}]$ calculations for the C_2H_6 (r_e = 1.53 Å) molecule at different inter-atomic distances. The orbitals are numbered and sorted according to their (CASSCF) natural occupation numbers. Strongly entangled orbitals are shown on the right-hand side. Each orbital index in the $s(1)_i$ diagram indicates one molecular orbital and corresponds to the same natural orbital as numbered in the mutual information plot (starting of index 1 and proceeding clockwise).

Paweł Tecmer

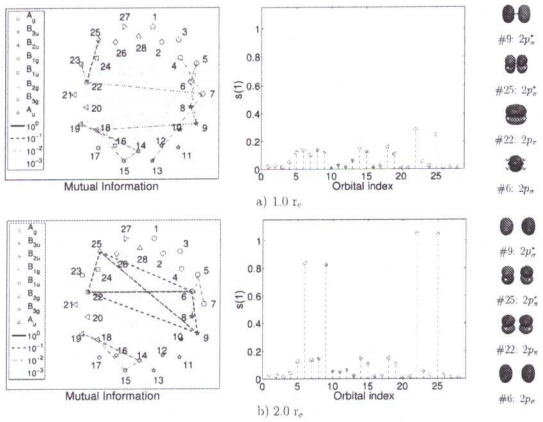

Figure 4: Mutual information and single orbital entropies $s(1)_i$ for DMRG(12,28)[$1024, 512, 10^{-5}$] calculations for the C_2H_4 (r_e = 1.34 Å) molecule at different inter-atomic distances. The orbitals are numbered and sorted according to their (CASSCF) natural occupation numbers. Strongly entangled orbitals are shown on the right-hand side. Each orbital index in the $s(1)_i$ diagram indicates one molecular orbital and corresponds to the same natural orbital as numbered in the mutual information plot (starting of index 1 and proceeding clockwise).

The quantum entanglement study of the C_2H_4 molecule determined from DMRG(12,28) wave functions is illustrated in Figure 4. We obtain a similar entanglement profile as for C_2H_6, though the bonding and anti-bonding p_π-orbitals

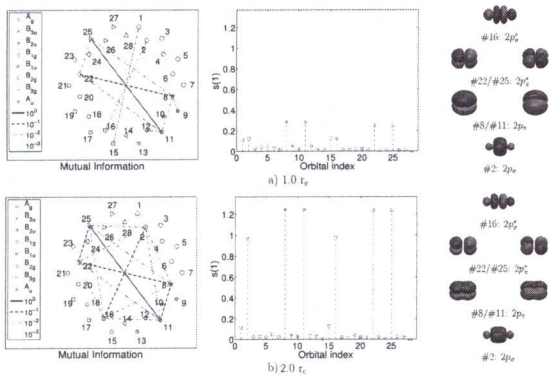

Figure 5: Mutual information and single orbital entropies $s(1)_i$ for DMRG(10,28)[$1024, 512, 10^{-5}$] calculations for the C_2H_2 (r_e = 1.21 Å) molecule at different inter-atomic distances. The orbitals are numbered and sorted according to their (CASSCF) natural occupation numbers. Strongly entangled orbitals are shown on the right-hand side. Each orbital index in the $s(1)_i$ diagram indicates one molecular orbital and corresponds to the same natural orbital as numbered in the mutual information plot (starting of index 1 and proceeding clockwise).

Paweł Tecmer

are now more strongly entangled around the equilibrium structure than the bonding and anti-bonding p_σ-orbitals. Pulling the CH_2 fragments apart, weakens first the π-bond followed by the (stronger) σ-bond. The entanglement-based bond order of carbon–carbon in the C_2H_4 molecule is equal to 2. The carbon–carbon bond in C_2H_2 is dissected in Figure 5. Similar to C_2H_4, four orbitals (#8, #11, #22 and #25) have slightly higher values for the single-orbital entropy than all remaining orbitals ($s(1)_i = 0.2$ vs. $s(1)_i = 0.1$) around the equilibrium distance. These are the doubly degenerate C $2p_\pi$- and C $2p_{\pi^*}$-orbitals. Stretching the CH fragments increases, as expected, first the orbital entanglement of the C $2p_\pi/2p_{\pi^*}$-orbitals, followed by the bonding and anti-bonding combination of the C $2p_z$ atomic orbitals. The entanglement diagram at $2.0r_e$ in the bottom panel of Figure 5 correctly predicts a triple bond between the two carbon centers in the C_2H_2 molecule.
In summary, our entanglement-based approach for determining bond orders, originally introduced for diatomic molecules, is transferable to polyatomic molecules and correctly predicts single, double, and triple bond orders between the carbon–carbon centers in ethane, ethene, and acetylene, respectively.

Monitoring reaction processes in the Ni-ethene complex. The formation of a metal–olefin bond is made possible through the process of back-donation, in which nickel d-orbitals push electrons into the π^*-orbitals of ethene (see Figure 6(b)). The back-bonding phenomenon is commonly understood using molecular orbital diagrams, where filled metal d-orbitals interact with empty ligand π^*-orbitals. This donation of electrons from metal to ligand causes a flow of electron density towards the ligands. Molecular orbital theory, however, restricts the understanding of back-donation to a rather simplified and solely qualitative picture, hampering a detailed analysis of metal–ligand bond-formation processes and the specific role of back-bonding therein. To obtain a trustworthy qualitative picture, one first must perform accurate computational studies, and then post-process the complicated information encoded in the correlated wave function in a way that facilitates chemical interpretation. In case of entanglement-based analysis, however, the information about orbital interactions can be easily obtained from the DRMG method without further post-processing data. Specifically, if two reactants approach each other, molecular orbitals that are involved in the bond formation process become strongly entangled. An orbital entanglement analysis is, thus, ideal to study molecular reactions because it allows us to identify

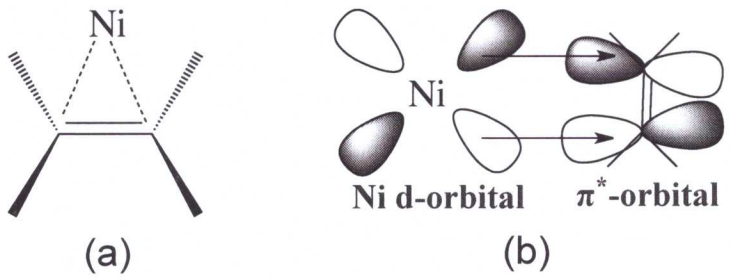

Figure 6: (a) Lewis structures of nickel-ethene. (b) Schematic representation of back-donation.

Paweł Tecmer

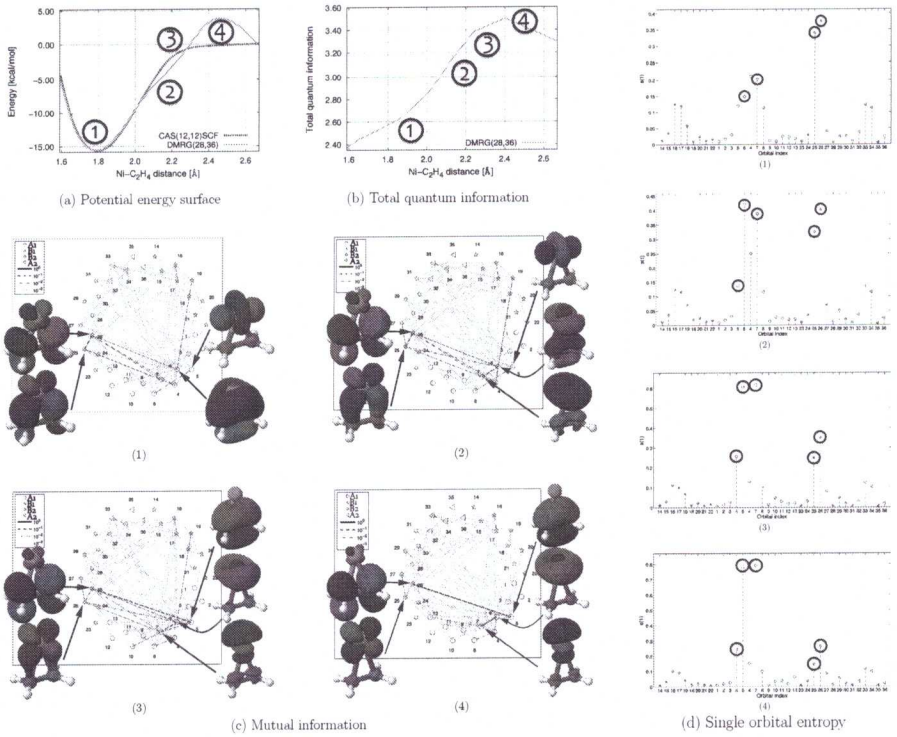

(a) Potential energy surface (b) Total quantum information

(c) Mutual information (d) Single orbital entropy

Figure 7: (a) Potential energy surface and (b-d) quantum information analysis of nickel-ethene complexation with respect to selected nickel-ethene distances. The chosen distances (1-4) are marked in (a) and cover the transition state (1), and the equilibrium distance (4). Molecular orbitals are marked by different symbols (according to their irreducible representation) in the mutual information and single orbital entropy diagrams. Highly correlated/entangled orbitals are highlighted in (c) and (d).

and monitor the most important orbital interactions along the reaction coordinate. By analyzing the mutual information and single orbital entropy diagrams, we are able to decide which orbital interactions form first and at which points of the dissociation pathway orbitals start communicating with each other.

In **[H5]**, we investigated the reaction pathway of nickel-ethene complexation (see Figure 6(a)) using quantum chemistry methods and demonstrated that the bond-formation process of nickel-ethene can be resolved by means of orbital entanglement. Specifically, orbital entanglement allowed us to determine exactly when back-donation starts to occur, and at which point of the reaction coordinate the bond between nickel and ethene forms. To react with ethene, the nickel atom has to undergo a spin-state change from a triplet (ground state of the free atom) to a singlet. Potential energy surfaces determined from CAS(12,12)SCF and DMRG are shown in Figure 7(a). While there is no energetic barrier to association at the CAS(12,12)SCF level, the DMRG potential energy surface predicts a transition state around a stretched nickel-ethene distance of 2.50 Å. Specifically, CAS(12,12)SCF fails to locate the correct electronic state as the distance between the nickel atom and the carbon atoms increases. This qualitative error in the CAS(12,12)SCF wave function is reflected in

Paweł Tecmer

the natural orbital occupation numbers. While CAS(12,12)SCF predicts occupation numbers of 1.30 and 0.70 for the $4s^1 3d^9$ (^{1}D) nickel orbitals, DMRG yields occupation numbers of 1.00. The presence of the transition state is also supported by quantum information theory. As emphasized in Refs. 52, the behaviour of the total quantum information—the sum of all single orbital entropies,[53]

$$I_{\text{tot}} = \sum_i s(1)_i, \tag{11}$$

as a function of bond distance allows us to detect and locate points where the electronic wave function changes drastically. Figure 7(b) shows the evolution of the total quantum information with respect to the nickel-ethene bond length. If the nickel atom and ethene molecule are pulled apart, the total quantum information increases gradually, up to a nickel-ethene distance of 2.4 Å. Beyond this point, the total quantum information decreases indicating the transition state, in which the wave function has a strong multi-reference character.
The orbital entanglement diagrams for selected points of the dissociation pathway are collected in Figures 7(c) and 7(d). Furthermore, molecular orbitals that are involved in the bond formation process, including π-donation and back-donation are highlighted in the mutual information diagram.
Close to the dissociation limit, the valence nickel and ethene orbitals are not entangled with each other and the strongly entangled orbitals are the ethene π/π^*-orbitals (nos. 5 and 26) as well as the nickel $3d_{z^2}/4s$-orbitals (nos. 6 and 7). If the ethene molecule approaches the nickel atom (point (4) of the reaction coordinate), the nickel $3d_{xz}$-orbital becomes entangled with the ethene π^*-orbital (nos. 25 and 26 in Figure 7(c-4)). Yet, the strongly entangled orbitals remain centred around the nickel atom and the ethene molecule. As the distance between nickel and ethene decreases and the system moves past the transition state (point (3) of the reaction coordinate), the nickel $3d/4s$-orbitals and the ethene π-orbital become strongly entangled (see Figure 7(c-3) and (d-3)) indicating the formation of the nickel-ethene bond through π-donation. Once the nickel-ethene distance decreases to approximately 2.15 Å (point (2) of the reaction coordinate), we observe a transition of orbital entanglement where the pair of bonding and anti-bonding orbitals involved in back-donation as well as orbitals involved in π-donation (the nickel $3d_{z^2}/4s$- and ethene π-orbitals) become highly entangled. At this point, the orbital entanglement is dominated by the bonding interaction between the nickel atom and the ethene molecule, while, around the equilibrium distance, only orbitals involved in back-donation (nos. 25 and 26) remain strongly entangled. Thus, in the case of nickel-ethene complexation, metal-ligand bonding is initialized by back-donation, which establishes around the transition state. This back-bonding then entails π-donation from the ethene ligand to the metal center.

Elucidating the dissociation process of $[UO_2]^{2+}$. The uranyl cation ($[UO_2]^{2+}$) constitutes the most pervasive actinide oxide. This small building block is often found in larger actinide complexes and usually adopts a linear geometry. In **[H4]**, we investigated the entanglement diagrams and electron correlation effects upon dissociation of ThO_2 and $[UO_2]^{2+}$ using the AP1roG model with optimized orbitals. The advantage

Paweł Tecmer

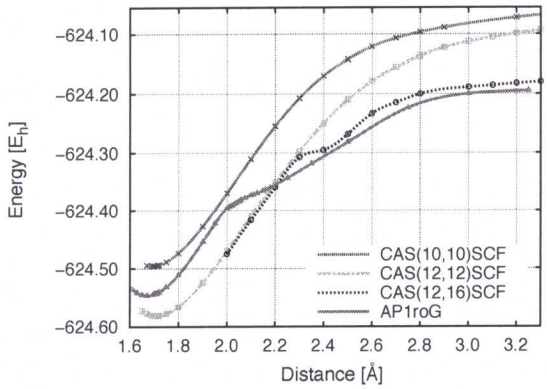

Figure 8: AP1roG and CASSCF potential energy surfaces for the symmetric dissociation of $[UO_2]^{2+}$.

of AP1roG over conventional CC-based and DFT methods is its ability to dissociate multiple bonds.[49,50,54] This is also the case for $[UO_2]^{2+}$, where only CASSCF and AP1roG calculations converged at distances larger than 2.10 Å. The resulting potential energy surfaces for the symmetric dissociation of the U-O bonds are presented in Figure 8. CAS(10,10)SCF and CAS(12,12)SCF give similar potential energy surfaces, that differ qualitatively from the CAS(12,16)SCF and AP1roG potential energy surfaces. While the smaller active space calculations result in potential energy surfaces without a plateau, the inclusion of non-bonding uranium ϕ_u and δ_u orbitals in CAS(12,16)SCF gives a potential energy surface with a shoulder at 2.4 Å. The AP1roG potential energy curve features two successive shoulders at 2.00 Å and at 2.10 Å, respectively.

To better understand the bonding situation and explain the origin of the double shoulder potential energy surface in $[UO_2]^{2+}$, we performed an orbital entanglement analysis[47,55] and analysed valence orbitals and their natural occupation numbers at various distances. Figure 9 depicts all orbitals with significant values of the single-orbital entropy $s(1)_i$. At the equilibrium distance all orbitals are only weakly entangled (cf. Figure 9(a)), with dominant contributions of orbitals 18-29. These are the molecular orbitals that participate in bonding, i.e., linear combinations of oxygen atomic p orbitals and uranium atomic f_π and f_σ orbitals. At this U–O distance the $[UO_2]^{2+}$ molecule can be well represented by a single-reference method as all the natural occupation numbers are close to 0 or 2. When the two oxygen atoms are pulled apart from the uranium center, orbitals 22-25 become strongly entangled. At a distance of 2.00 Å, orbitals 23 and 24 (π-type orbitals involved in bonding) have the largest value of $s(1)_i$. Molecular orbitals 22 and 25 are composed of atomic uranium f_σ and oxygen p_σ orbitals. Passing the first shoulder on the potential energy surface, at 2.01 Å (cf. Figure 9(c)), the electronic structure changes. From this distance onward, the characteristic non-bonding ϕ orbitals of uranium become occupied, suggesting their importance in CASSCF calculations during the dissociation process. At 2.11 Å (the second shoulder), the uranium f_σ-orbital does not participate

Paweł Tecmer

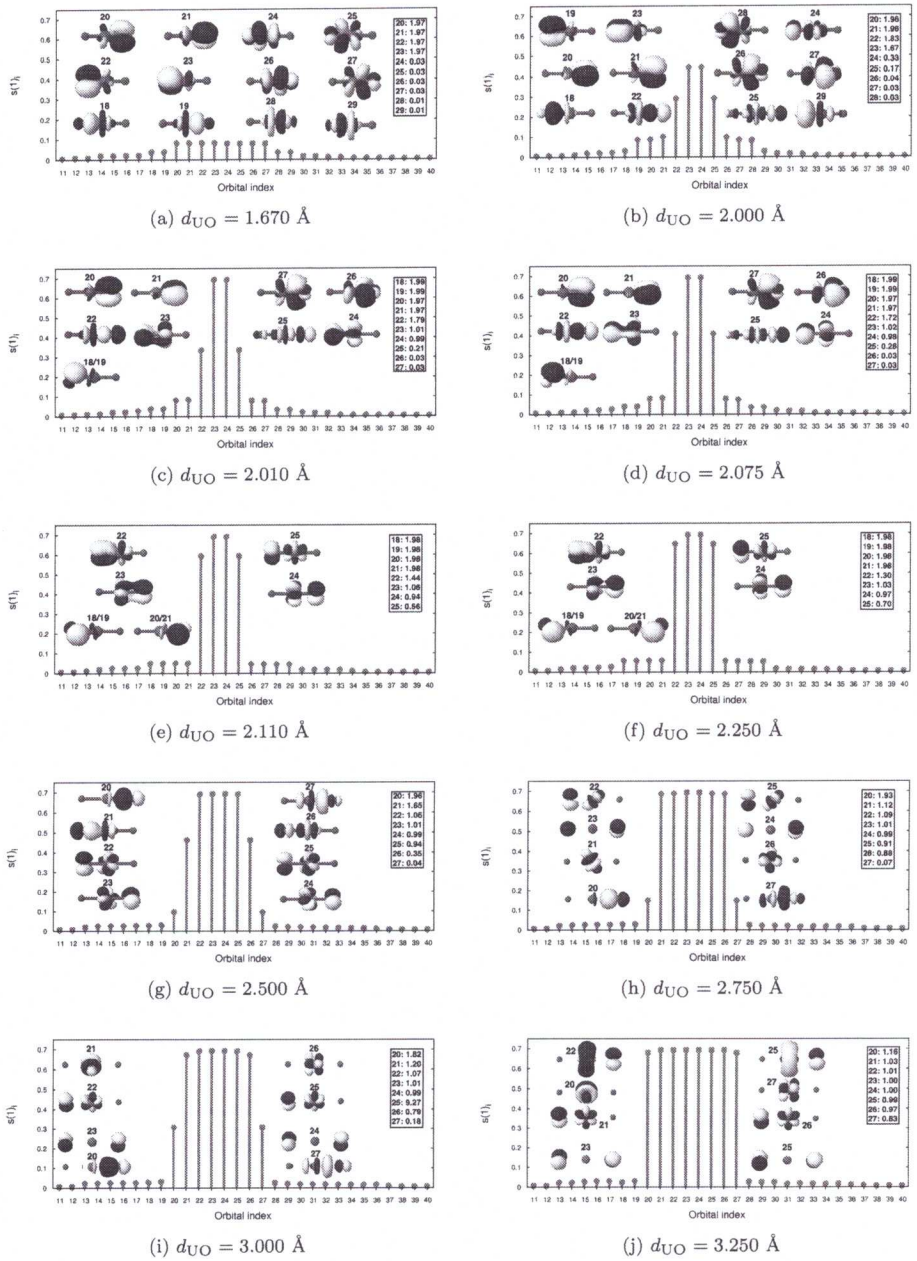

(a) $d_{UO} = 1.670$ Å (b) $d_{UO} = 2.000$ Å

(c) $d_{UO} = 2.010$ Å (d) $d_{UO} = 2.075$ Å

(e) $d_{UO} = 2.110$ Å (f) $d_{UO} = 2.250$ Å

(g) $d_{UO} = 2.500$ Å (h) $d_{UO} = 2.750$ Å

(i) $d_{UO} = 3.000$ Å (j) $d_{UO} = 3.250$ Å

Figure 9: Comparison of AP1roG single-orbital entropies $s(1)_i$, valence orbitals, and their natural occupation numbers for the $[UO_2]^{2+}$ molecule at different inter-atomic distances.

in bonding any more (cf. Figure 9(e)). Hence, the double-shoulder potential energy surface of $[UO_2]^{2+}$ results from different bonding patterns at 2.00 Å and 2.10 Å, respectively. Pulling the oxygen atoms further apart from the uranium center, the number of singly-occupied orbitals with large values of $s(1)_i$ gradually increases (cf. Figures 9(f)–9(i)). At 2.75 Å, there are 6 maximally entangled orbitals (21-26). These

Paweł Tecmer

are the uranium f and oxygen p atomic orbitals. Finally, at around 3.25 Å, the U–O bonds are fully dissociated with 8 maximally entangled singly occupied orbitals. As shown in Figure 9(j), AP1roG predicts uranium to have charge 2+ and the [Rn]:$5f^3 7s^1$ electronic configuration in the dissociation limit.

In search of optimal active spaces in multi-reference plutonium complexes. The electronic structures of $[PuO_2]^{2+}$ and PuO_2, small building blocks of larger, more realistic plutonium containing-compounds, have been intensively studied in the past.[56–59] However, a reliable modeling of the electronic structure of larger plutonium compounds remains a real challenge for present day quantum chemistry mainly due to their strong multi-reference nature. This problem has been addressed in **[H2]**, where the electronic structure of various plutonium oxides such as $[PuO_2]^{2+}$, PuO_2, PuO_3 and $PuO_2(OH)_2$ have been investigated using the DMRG algorithm. Specifically, for the PuO_3 and $PuO_2(OH)_2$ molecules two sets of calculations have been carried out, one with the full valence CAS orbitals denotes as FV-CAS and another one with selected optimal orbital CAS denoted as optCAS. The corresponding orbital correlations are depicted in Figure 10.

The PuO_3 compound. The plutonium δ_u ($6b_2 \oplus 2a_2$) and ϕ_u ($8a_1 \oplus 4b_1$) orbitals of PuO_3 are highly correlated with each other, while the remaining active space orbitals are moderately to weakly correlated (see Figure 10(a)), especially like the σ_u–σ_u^* ($4b_2/7b_2$) and π_u–π_u^* ($5a_1 \oplus 2b_1/11a_1 \oplus 6b_1$) orbital pairs that fall below the threshold of 10^{-1} in the optCAS. Although weak correlations ($I_{i|j} \leq 10^{-2}$) are underestimated in the optCAS calculations compared to the FV-CAS reference, optCAS still represents the smallest active space that contains all important orbitals to reliably describe nondynamic/static electron correlation.
An interesting feature concerns the orbitals that describe the bonding between the distorted plutonyl subunit and the most distant oxygen atom. The bonding and anti-bonding orbitals forming σ-type orbitals ($2a_1$ and $4a_1$; linear combinations of the most distant oxygen 2s and plutonium $6p_x$) are not important for the description of static/nondynamic electron correlation effects of the ground-state wave-function. The axial and equatorial oxygen p_x orbitals interact with the plutonium $6d_{x^2-y^2}$ orbital and the resulting molecular orbital ($\pi_d + p_x^{(O)}$) can be considered as a hybrid of an axial plutonium–oxygen σ bond and σ-type bonding between the three oxygen atoms. This σ-type molecular orbital is moderately correlated with the singly occupied plutonium ϕ_u orbital. The axial oxygen p_y orbital forms a π-type bond with the plutonyl π_g ($3b_1$) orbital. The remaining axial oxygen p_z orbital slightly mix with plutonium π_g ($5b_2$) and becomes moderately correlated with the plutonium ϕ_u and δ_u orbitals.
The strong discrepancies in $I_{i|j}$ between optCAS and FV-CAS can be explained by investigating the electronic structure of PuO_3. The electronic structure of PuO_3 is dominated by dynamic electron correlation effects beyond the optCAS orbitals, which results in $I_{i|j}$ being underestimated in comparison to the FV-CAS reference. However, the missing dynamic electron correlation effects do not considerably affect the nondynamic/static correlation in the (optCAS) active space and can be included *a posteriori* using, for instance, perturbation theory.

Paweł Tecmer

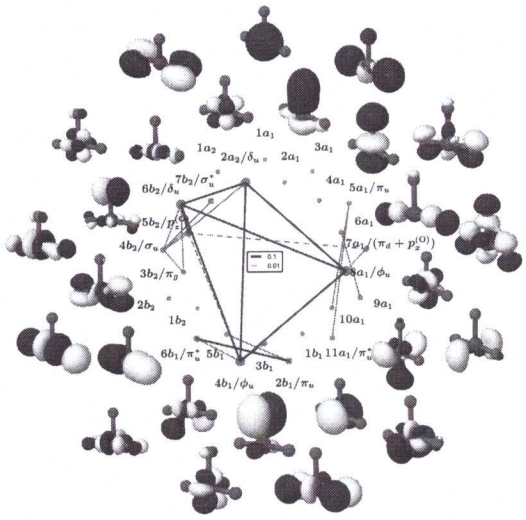

(i) FV-CAS

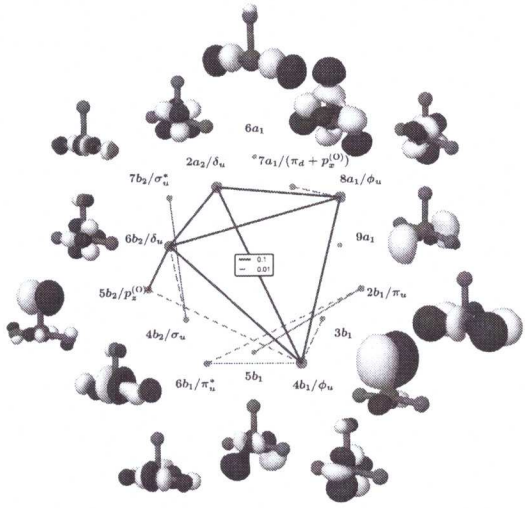

(ii) OptCAS

(a) PuO_3

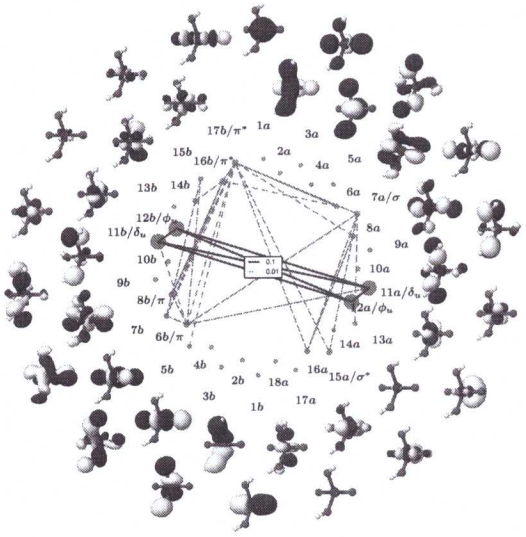

(i) FV-CAS

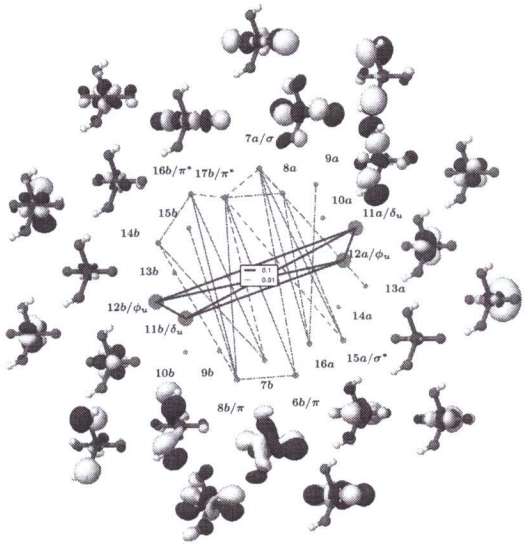

(ii) OptCAS

(b) $PuO_2(OH)_2$

Figure 10: Orbital correlations for the PuO_3 and $PuO_2(OH)_2$ molecules and two different active spaces. The strength of the orbital-pair correlations is color-coded: the strongest orbital-pair correlations are marked by blue lines (10^{-1}), followed by orbital-pair correlations linked by red lines (10^{-2}).

Note that nondynamic/static electron correlation effects can be accurately described within the optCAS (DMRG(14,14)), which contains the most distant-oxygen p orbitals and the other orbitals of the distorted plutonyl subunit. Hence, a minimal active space containing the σ_u/σ_u^*, π_u/π_u^*, π_d, and δ_u as well as ϕ_u orbitals and the

Paweł Tecmer

p-shell of the oxygen would suffice to accurately model the ground-state wave function in PuO_3.

The $PuO_2(OH)_2$ complex. As observed for the PuO_3 complex, extending the ligand sphere of $[PuO_2]^{2+}$ with two hydroxy groups changes the orbital-pair correlations compared to the triatomic subunit. In the $PuO_2(OH)_2$ molecule, the singly-occupied δ_u ($11a \oplus 11b$) and ϕ_u ($12a \oplus 12b$) orbitals are strongly correlated, while the plutonyl π and π^*-type orbitals ($6b$, $8b$, $16b$ and $17b$) are moderately correlated. To describe nondynamic/static electron correlation appropriately, the active space can be reduced from 35 (FV-CAS) to 22 (OptCAS) orbitals without changing orbital-pair correlations. The small discrepancies in $I_{i|j}$ between optCAS and FV-CAS can be attributed to dynamic correlations effects outside the optCAS active space. Thus, optCAS with 20 electrons correlated in 22 orbitals represents a good choice to describe the most important correlation effects present in the $PuO_2(OH)_2$ molecule.
The plutonium 5f/6d orbitals mix with the oxo p orbitals to form moderately correlated f/d_π and f/d_{π^*}-type orbitals ($6b$, $8b$, $16b$ and $17b$), while the hydroxy p orbitals mix with the oxo p orbitals and the plutonium 5f/6d orbitals to form molecular orbitals ($8a$ and $7b$) that are moderately correlated with the f/d_π and f/d_{π^*}-type orbitals. Finally, the hydroxy lone-pairs ($9a$, $10a$, $9b$, and $10b$) are only weakly correlated ($I_{i|j} < 10^{-2}$) with molecular orbitals centered on the $[PuO_2]^{2+}$ subunit, which are thus not shown in the Figure.
To summarize the work presented in **[H2]**, an optimal active space can be defined by only selecting the strongly correlated orbitals, from a large active space calculation that reproduces the orbital-pair correlation diagram of the reference calculation, resulting in DMRG(14,16) for linear $[PuO_2]^{2+}$, DMRG(18,17) for linear PuO_2, DMRG(14,14) for PuO_3, and finally DMRG(20,22) for $PuO_2(OH)_2$. Most importantly, the discrepancies in $I_{i|j}$ between optCAS and FV-CAS are minor and are caused by dynamic electron correlation effects beyond the optCAS active space orbitals. Thus, optCAS should result in reliable zeroth-order wave function for an *a posteriori* treatment of dynamic electron correlation effects.

Quantum entanglement effect of noble gas coordination on the spin state of CUO. The electronic structure of the bare CUO molecule bears considerable similarity to its isoelectronic analogs, $[UO_2]^{2+}$, $[NUO]^+$, and NUN[29,60–63], where the U $6p$-, $5f$- and $6d$-orbitals interact with the $2s$- and $2p$-orbitals of the lighter elements entailing a stable linear structure.[64] Yet, the energetically higher lying atomic orbitals of the C atom (in contrast to O and N) destabilize the CUO complex compared to the other isoelectronic species[65]. It is now well-established that the CUO molecule features a $^1\Sigma^+$ ground-state, which is very close in energy to a $^3\Phi$ excited state.[66–68] Our scalar-relativistic CAS(12,12)SCF (**[H8]**) calculation correctly predicts the $^1\Sigma^+$ state to be the ground state of the bare CUO molecule, which is separated by only 0.71 eV from the first adiabatically excited $^3\Phi$ state. This singlet–triplet splitting reduces to 0.60 eV in our scalar relativistic DMRG(14,40) calculations.
In **[H8]** the noble gas environment is represented by four noble gas atoms arranged in an equatorial plane with respect to the CUO axis as depicted in Figure 11. The

Paweł Tecmer

potential energy curves obtained from CASSCF and DMRG calculations are then fitted to a generalized Morse potential function and are plotted in Figure 12(a). Exploring Figure 12(a), we observe an overall stabilization of the CUO molecule upon complexation of both Ng_4 surroundings. The complexation energy strongly depends on the spin state and on the specific Ng ligand. While the potential well depth is rather shallow for the Ne_4 matrix, it is twice as large in the Ar_4 environment for all electronic states investigated. In general, DMRG predicts a larger interaction energy between CUO and the noble gas atoms than CASSCF, which is more pronounced in

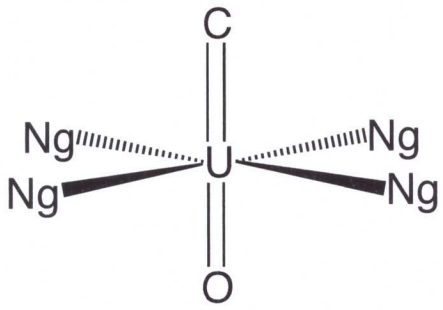

Figure 11: Lewis structure of $CUONg_4$ for Ng = Ne, Ar.

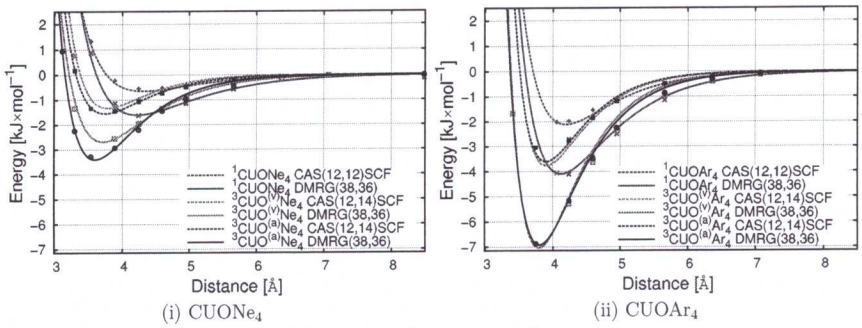

(i) $CUONe_4$ (ii) $CUOAr_4$

(a) Potential energy surfaces

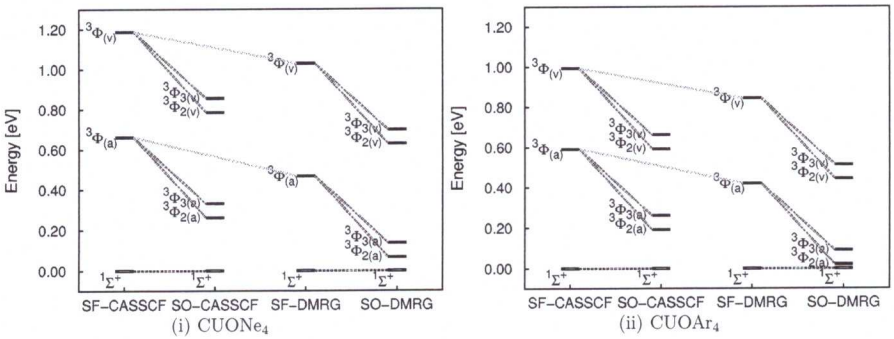

(i) $CUONe_4$ (ii) $CUOAr_4$

(b) Spin state splittings

Figure 12: Potential energy curves and spin-state splittings for $CUONg_4$. (a) Reconstructed potential energy surfaces of (i) $CUONe_4$ and (ii) $CUOAr_4$ in $kJmol^{-1}$. (b) Spin-free (SF) and spin–orbit (SO) corrected spin-state splittings of (i) $CUONe_4$ and (ii) $CUOAr_4$ in eV.

Pawel Tecmer

the case of the Ar_4 than for the Ne_4 environment.
It is important to note that the interaction energy is similar for the vertically and the adiabatically excited states of $CUOAr_4$. The shortest U–Ng bond length is found for $^3\Phi$ $CUOAr_4$, while the longest bond distance is observed for $^1\Sigma^+$ $CUONe_4$. For both Ng_4 environments, the equilibrium bond distances determined in DMRG calculations are generally shorter than for CASSCF.
Figure 12(b) illustrates the changes of the spin-state splittings induced by the surrounding noble gases. As adiabatically excited states are lower in energy than the vertically excited states, the adiabatic energy difference yields the smallest singlet–triplet gaps. The spin-free CASSCF spin-state splitting of 0.66 eV in the Ne_4 surrounding is reduced to 0.59 eV in the Ar_4 environment. Similarly, the spin-free DMRG singlet–triplet gap of 0.47 eV determined for $CUONe_4$ decreases to 0.42 eV for $CUOAr_4$. A perturbative correction for spin–orbit coupling further lowers the $^3\Phi_{2(a)}$ state to approach the $^1\Sigma_0^+$ state. For CASSCF, the energy gap of $^3\Phi_{2(a)}$ and $^1\Sigma_0^+$ is lowered to 0.26 and 0.19 eV for $CUONe_4$ and $CUOAr_4$, respectively, while it reduces to 0.07 and 0.02 eV, respectively, in the DMRG calculations. In particular, an energy gap of 0.02 eV is below "chemical accuracy", which is of the order of 0.04 eV (or 4 kJ/mol), and hence the $^1\Sigma_0^+$ and $^3\Phi_{2(a)}$ states can be considered as energetically equivalent, where a thermal spin crossover ($^1CUOAr_4 \leftrightarrow {}^3CUO^{(a)}Ar_4$) is possible. Although,

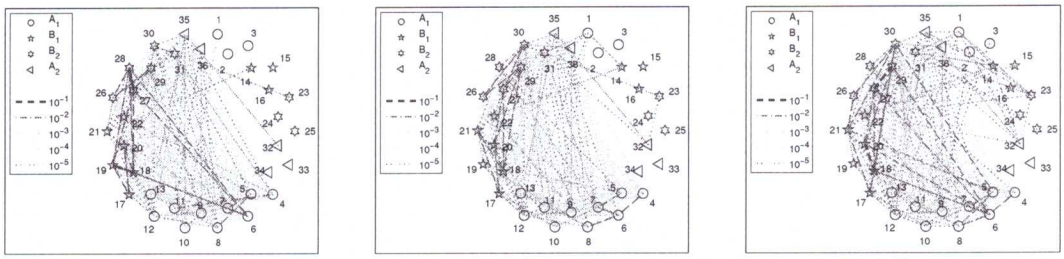

(i) $^1\Sigma^+$ (ii) $^3\Phi_{(v)}$ (iii) $^3\Phi_{(a)}$

(a) $CUONe_4$

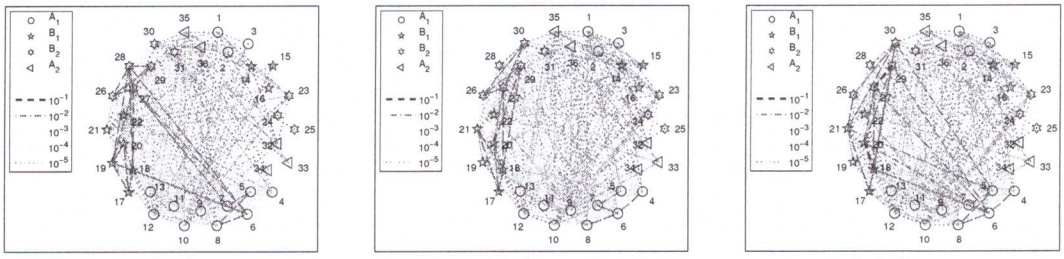

(i) $^1\Sigma^+$ (ii) $^3\Phi_{(v)}$ (iii) $^3\Phi_{(a)}$

(b) $CUOAr_4$

Figure 13: Quantum entanglement analysis of the CUO-Ng_4 (Ng = Ne, Ar) interaction. Mutual information of $CUONg_4$ orbital pairs determined at the equilibrium U–Ng distances. The first twelve orbitals represent Ng_4 molecular orbitals, while the remaining molecular orbitals are centered on the CUO moiety. $^3\Phi_{(v)}$: $^3\Phi$ state for $CUO^{(v)}Ng_4$. $^3\Phi_{(a)}$: $^3\Phi$ state for $CUO^{(a)}Ng_4$.

Paweł Tecmer

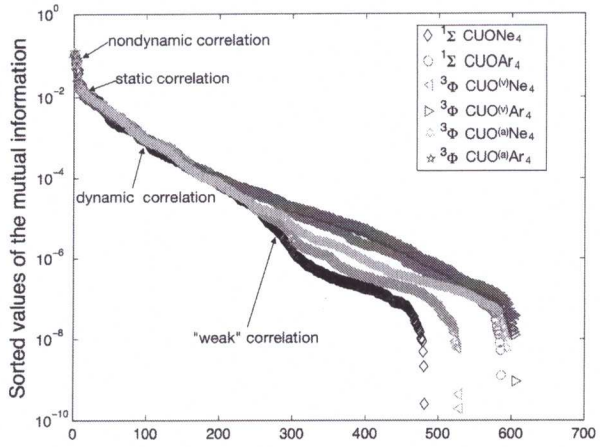

Figure 14: Decay of mutual information for $CUONe_4$ and $CUOAr_4$ in different spin states.

the complexation of the CUO molecule by the noble gas ligands is small, its effect on the spin-state splittings is remarkable and asks for an analysis of the quantum entanglement among the single-electron states. Figure 13 shows the mutual information which is color-coded: nondynamic electron correlation is indicated by blue (mutual information of order $\sim 10^{-1}$) and static by red (mutual information of order $\sim 10^{-2}$) connecting lines, while dynamic correlation is mainly attributed to orbitals connected by green (mutual information of order $\sim 10^{-3}$) lines.

The entanglement between the Ng_4 molecular orbitals and those molecular orbitals centered on the CUO unit is considerably weaker than between molecular orbital pairs centered on CUO only. In particular, the weakest interaction i.e., the smallest number of purple lines between Ng_4 molecular orbitals and CUO-centered molecular orbitals is found for $^1\Sigma^+$ $CUONe_4$, but gradually increases when going from $^3\Phi$ $CUO^{(v)}Ne_4$ to $^3\Phi$ $CUO^{(a)}Ne_4$. The differences in orbital correlations are more clearly illustrated in Figure 14 where the values of the mutual information are plotted in descending order for all investigated $CUONg_4$ compounds. While the decay of $I_{i,j}$ is similar for all $CUONg_4$ complexes if $I_{i,j} \geq 10^{-4}$, the evolution of the mutual information forks at $I_{i,j} \approx 10^{-4}$. Thus, different orbital entanglement patterns are obtained for small-valued $I_{i,j}$. All CUO complexes with argon atoms contain more weakly entangled orbitals ($I_{i,j} < 10^{-4}$) than CUO compounds in the Ne_4 surrounding. In addition, the decay of $I_{i,j}$ is in general faster for the $^1\Sigma$ state than for the $^3\Phi$ configuration of the CUO molecule.

These entanglement patterns support the increasing potential well depth for $^1\Sigma^+$, over $^3\Phi$ $CUO^{(v)}Ne_4$ to $^3\Phi$ $CUO^{(a)}Ne_4$ as shown in Figure 12(a). A qualitatively and quantitatively different entanglement picture is obtained for $CUOAr_4$, where a strong interaction between the CUO unit and the Ar_4 surrounding is already present for the $^1\Sigma^+$ state and further increases when going from $^3\Phi$ $CUO^{(v)}Ar_4$ to $^3\Phi$ $CUO^{(a)}Ar_4$. Since the interaction of the Ne_4 and Ar_4 surrounding with the CUO unit is very weak, the single orbital entropies of the noble gas molecular orbitals are close to Zero, while the single-orbital entropies corresponding to CUO-centered molecular orbitals

Paweł Tecmer

are considerably larger. Large values of the single-orbital entropy indicate that the electronic structure of the CUO unit is dominated by static electron correlation. However, we should note that the single-orbital entropy corresponding to the noble gas molecular orbitals are nevertheless larger for $CUOAr_4$ than for $CUONe_4$ due to the stronger interaction of the CUO unit with the Ar_4 surrounding. Since the structure of the CUO unit is similar for both $CUONe_4$ and $CUOAr_4$, these discrepancies can only be related to the change in the noble gas surrounding and thus support that the orbital entanglement between Ng_4 and CUO is stronger for Ar_4 than for Ne_4.
In summary, our entanglement study using mutual information points to different quantum correlations of the weakly coordinating noble-gas atoms by which the "mysterious" interaction of CUO with Ne_4 and Ar_4 can be explained. In particular, the total quantum information I_{tot} comprised in the $CUONe_4$ and $CUOAr_4$ molecules indicates larger quantum entanglement of the Ar_4 orbitals with the CUO-centered molecular orbitals compared to the Ne_4 environment.

c.4 Different schemes to include spin–orbit coupling

It is a well-established fact that spin–orbit interactions are essential to reach spectroscopic accuracy.[7,69,70] Unfortunately, an accurate four-component Dirac–Coulomb (DC) Hamiltonian has the downside of increased computational expense, notably for the AO–MO transformation step for correlated calculations. This high computational cost is a limiting factor to investigate larger molecular systems with accurate correlation methods. An alternative is found in two-component approaches, in which the large and small components will be decoupled and solutions can be expressed in terms of the large-component functions only.[69] A particularly interesting two-component method is based on the so-called "eXact 2-Component"[71] (X2C) which can provide an exact decoupling for the matrix representation of the Hamiltonian. However, in order to construct the decoupling, one needs solutions for a coupled system. This drawback has motivated the development of two main computational schemes: one based on the decoupling in an atomic mean-field[72] (AMF) fashion, and another in which the decoupling is based on the molecular four-component solutions,[73] with two-electron interactions being approximated in a molecular mean-field (MMF) fashion. The AMF approach is computationally more advantageous than the MMF, since only two-electron integrals over large component basis functions are required at the SCF step, but at the cost of discarding multi-center contributions to the spin–orbit interactions.
Another relativistic effect worth considering for actinides is the Gaunt (G) interaction,[74] which describes the magnetic interaction between the spin current of one electron and the orbital current of another one[69]. In **[H6]**, the importance of both spin–orbit coupling and the (approximate) Gaunt interactions on the electronic structure of the $[UO_2]^{2+}$, $[NUO]^{+}$, and NUN isoelectronic series is highlighted.
The spin–orbit coupling electronic spectra obtained from the IH-FSCCSD approach using different relativistic Hamiltonians are compiled in Table 1 ($[UO_2]^{2+}$), Table 2 ($[NUO]^{+}$), and Table 3 (NUN). The low-lying electronic excitations in the uranyl cation ($[UO_2]^{2+}$) are dominated by transitions from the occupied $\sigma^{(O)}_{1/2u}$- and $\pi^{(O)}_{1/2u}$-spinors to the nonbonding $\phi^{(U)}_{5/2u}$-, $\phi^{(U)}_{7/2u}$-, $\delta^{(U)}_{3/2u}$- and $\delta^{(U)}_{5/2u}$-spinors. In the upper part of

Paweł Tecmer

Table 1: 15 lowest-lying IH-FSCCSD vertical excitation energies of the $[UO_2]^{2+}$ molecule ($r_{U-O} = 1.708$ Å). Excitation energies are given in eV.

Ω	character (from DC)	DC	DC(G)	X2C/AMF	X2C/MMF	X2C(G)/MMF
2_g	65% $\sigma_{1/2u}\phi_{5/2u} + 17\%\ \pi_{1/2u}\phi_{5/2u}$	1.764	1.727	1.741	1.765	1.728
1_g	70% $\sigma_{1/2u}\delta_{3/2u} + 20\%\ \pi_{1/2u}\delta_{3/2u}$	1.843	1.801	1.819	1.843	1.801
3_g	66% $\sigma_{1/2u}\phi_{5/2u} + 18\%\ \pi_{1/2u}\phi_{5/2u}$	1.919	1.880	1.896	1.919	1.881
2_g	47% $\sigma_{1/2u}\delta_{3/2u} + 20\%\ \sigma_{1/2u}\delta_{5/2u}$	2.131	2.085	2.108	2.131	2.085
3_g	65% $\sigma_{1/2u}\delta_{5/2u} + 22\%\ \pi_{1/2u}\delta_{5/2u}$	2.514	2.453	2.491	2.513	2.452
4_g	72% $\sigma_{1/2u}\phi_{7/2u} + 20\%\ \pi_{1/2u}\phi_{7/2u}$	2.592	2.532	2.571	2.592	2.532
3_g	65% $\sigma_{1/2u}\phi_{7/2u}$	2.992	2.938	2.972	2.992	2.938
2_g	50% $\sigma_{1/2u}\delta_{5/2u} + 22\%\ \sigma_{1/2u}\delta_{3/2u}$	3.394	3.346	3.374	3.394	3.346
1_g	96% $\pi_{3/2u}\phi_{5/2u}$	3.853	3.817	3.829	3.853	3.817
4_g	97% $\pi_{3/2u}\phi_{5/2u}$	3.968	3.932	3.945	3.968	3.933
3_g	97% $\pi_{3/2u}\delta_{3/2u}$	4.079	4.042	4.056	4.079	4.042
2_u	81% $\sigma_{1/2g}\phi_{5/2u} + 16\%\ \sigma_{1/2g}\delta_{3/2u}$	4.084	4.038	4.057	4.084	4.039
0_g^-	96% $\pi_{3/2u}\delta_{3/2u}$	4.086	4.049	4.064	4.087	4.049
0_g^+	96% $\pi_{3/2u}\delta_{3/2u}$	4.122	4.082	4.098	4.122	4.082
3_u	98% $\sigma_{1/2g}\phi_{5/2u}$	4.125	4.079	4.099	4.125	4.080

Table 2: 15 lowest-lying IH-FSCCSD vertical excitation energies of the $[NUO]^+$ molecule ($r_{U-O} = 1.761$ Å, $r_{U-N} = 1.698$ Å). Excitation energies are given in eV.

Ω	character (from DC)	DC	DC(G)	X2C/AMF	X2C/MMF	X2C(G)/MMF
2	71% $\sigma_{1/2}\phi_{5/2} + 15\%\ \sigma'_{1/2}\phi_{5/2}$	1.018	0.987	1.001	1.020	0.992
3	69% $\sigma_{1/2}\phi_{5/2}$	1.147	1.114	1.130	1.149	1.120
1	68% $\sigma_{1/2}\delta_{3/2} + 15\%\ \sigma'_{1/2}\delta_{3/2}$	1.215	1.179	1.197	1.216	1.183
2	54% $\sigma_{1/2}\delta_{3/2}$	1.440	1.401	1.423	1.441	1.405
4	72% $\sigma_{1/2}\phi_{7/2} + 15\%\ \sigma'_{1/2}\phi_{7/2}$	1.778	1.725	1.762	1.779	1.728
3	69% $\sigma_{1/2}\delta_{5/2}$	1.811	1.758	1.794	1.811	1.760
3	62% $\sigma_{1/2}\phi_{7/2}$	2.101	2.052	2.086	2.102	2.056
2	57% $\sigma_{1/2}\delta_{5/2}$	2.361	2.316	2.345	2.362	2.319
1	96% $\pi_{3/2}\phi_{5/2}$	2.656	2.621	2.640	2.662	2.630
4	97% $\pi_{3/2}\phi_{5/2}$	2.743	2.708	2.726	2.748	2.716
3	83% $\pi_{1/2}\phi_{5/2}$	2.932	2.894	2.918	2.937	2.903
0^-	93% $\pi_{3/2}\delta_{3/2}$	2.947	2.911	2.932	2.953	2.919
3	88% $\pi_{3/2}\delta_{3/2}$	2.987	2.950	2.971	2.992	2.958
0^+	93% $\pi_{3/2}\delta_{3/2}$	2.988	2.949	2.973	2.993	2.957
2	82% $\pi_{1/2}\phi_{5/2}$	3.016	2.966	2.991	3.010	2.974

the spectrum, electrons are excited from the lower occupied $\sigma^{(O)}_{1/2g}$- and $\pi^{(O)}_{3/2u}$-spinors.

Similar to $[UO_2]^{2+}$, in the $[NUO]^+$ molecule low-lying excitations occur mostly from the light element (the nitrogen atom) to the uranium atom (see Table 2). Both electronic spectra are well described by electronic transitions from the occupied $\sigma^{(N)}_{1/2}$- and $\sigma'^{(N)}_{1/2}$-spinors in the lower part, and $\pi^{(N)}_{3/2}$- and $\pi^{(N)}_{1/2}$-spinors in the upper part to the nonbonding $\phi^{(U)}_{5/2}$-, $\phi^{(U)}_{7/2}$-, $\delta^{(U)}_{3/2}$- and $\delta^{(U)}_{5/2}$-spinors. A significant difference is, however, that the low-lying excited states in the $[NUO]^+$ molecule lie much lower in

Paweł Tecmer

Table 3: 15 lowest-lying IH-FSCCSD vertical excitation energies of the NUN molecule (r_{U-N} = 1.739 Å). Excitation energies are given in eV.

Ω	character (from DC)	DC	DC(G)	X2C/AMF	X2C/MMF	X2C(G)/MMF
2_g	52% $\sigma_{1/2u}\phi_{5/2u}$ + 26% $\pi_{1/2u}\phi_{5/2u}$	0.956	0.923	0.936	0.957	0.927
3_g	50% $\sigma_{1/2u}\phi_{5/2u}$ + 24% $\pi_{1/2u}\phi_{5/2u}$	1.103	1.068	1.083	1.103	1.072
1_g	45% $\sigma_{1/2u}\delta_{3/2u}$ + 20% $\pi_{1/2u}\delta_{3/2u}$	1.134	1.094	1.106	1.134	1.098
2_g	30% $\sigma_{1/2u}\delta_{3/2u}$ + 15% $\pi_{1/2u}\delta_{3/2u}$	1.398	1.355	1.374	1.398	1.358
4_g	49% $\sigma_{1/2u}\phi_{7/2u}$ + 23% $\pi_{1/2u}\phi_{7/2u}$ + 16% $\sigma_{1/2u}\phi'_{7/2u}$	1.699	1.645	1.680	1.698	1.646
3_g	43% $\sigma_{1/2u}\delta_{5/2u}$ + 20% $\pi_{1/2u}\delta_{5/2u}$	1.757	1.704	1.739	1.757	1.705
3_g	38% $\sigma_{1/2u}\phi_{7/2u}$ + 22% $\pi_{1/2u}\phi_{7/2u}$	2.076	2.028	2.059	2.076	2.029
2_g	33% $\sigma_{1/2u}\delta_{5/2u}$ + 17% $\pi_{1/2u}\delta_{5/2u}$	2.519	2.476	2.502	2.519	2.478
1_u	40% $\sigma_{1/2u}\delta_{3/2g}$ + 24% $\pi_{1/2u}\delta_{3/2g}$	2.669	2.696	2.680	2.669	2.696
0_u^+	41% $\sigma_{1/2u}\sigma_{1/2g}$ + 30% $\pi_{1/2u}\sigma_{1/2g}$	2.709	2.757	2.740	2.709	2.755
1_u	41% $\pi_{3/2u}\sigma'_{1/2g}$ + 29% $\pi'_{3/2u}\sigma''_{1/2g}$	2.711	2.759	2.743	2.711	2.757
1_g	80% $\pi_{3/2u}\phi_{5/2u}$	2.711	2.675	2.690	2.711	2.679
2_u	34% $\sigma_{1/2u}\delta_{3/2g}$ + 24% $\pi_{1/2u}\delta_{3/2g}$	2.749	2.767	2.758	2.749	2.768
4_g	84% $\pi_{3/2u}\phi_{5/2u}$	2.844	2.808	2.823	2.844	2.811
2_u	73% $\sigma_{1/2g}\phi_{5/2u}$	2.895	2.857	2.875	2.895	2.860

energy than in $[UO_2]^{2+}$ (ca. 0.7 eV).
The electronic states for NUN are quite distinct from those for $[UO_2]^{2+}$, and $[NUO]^+$, in that they possess very pronounced multi-reference character (cf. Table 3) and show a relatively low-lying state (0_u^+ at 2.7 eV) in which electrons in NUN can be transferred to spinors centered solely on the nitrogen atom. That said, for all species the eight lowest-lying electronic transitions involve the same unoccupied uranium spinors, with transition energies being rather similar (compare Tables 2 and 3) and showing the same ordering with respect to Ω for NUN and $[NUO]^+$, but lower than the corresponding ones in $[UO_2]^{2+}$ by about 0.7–0.8 eV.
The distinctive features of the NUN electronic structure with respect to $[NUO]^+$ or $[UO_2]^{2+}$ originate from differences both in the occupied spinors (which are delocalized over the uranium and nitrogen atoms) and the lowest unoccupied spinors. The importance of the latter can be better understood by comparing the electronic structures of the Uranium(V) species: while the $[UO_2]^+$ and NUO molecules bear the same ground state electronic configuration ($\sigma^2_{1/2u}\phi^1_{5/2u}$ and $\sigma^2_{1/2}\phi^1_{5/2}$, respectively) and in both cases low-lying electronic excitations occur to the unoccupied uranium ϕ- and δ-spinors as in the Uranium(VI) species, the NUN^- moiety exhibits a totally different ground state electronic configuration ($\sigma^2_{1/2u}\sigma^1_{1/2g}$) and other type of spinors are involved in low-lying excitations. Excitation energies calculated from the DC Hamiltonian and those from the approximate X2C/AMF and X2C/MMF Hamiltonians are similar for all molecules investigated in this work. The overall agreement of the X2C/MMF data with the DC data is very good for all molecules and discrepancies are usually smaller than 0.002 eV (cf. Tables 1–3). Yet, the advantage of X2C/MMF over DC is reduced CPU time required for the four-index transformation, a bottleneck of correlated calculations. The errors originating from the X2C/AMF approximation amount up to 0.03 eV which may be acceptable since this approach provides further computational savings. The presence of Gaunt interactions in the DC Hamiltonian causes changes in the excitation energies on the order of 0.03–0.07 eV for all molecules. Notably, the X2C(G)/MMF results are almost indistinguishable from the reference DC(G) results.

Paweł Tecmer

c.5 Bridging the gap between theory and experiment

The thorium monoxide (ThO) molecule, has been pointed out as a candidate in the search of the electron electric dipole moment (eEDM).[75,76] As a result, both experimental and theoretical groups set sights on the reliable description of the ground and electronically excited states of the ThO molecule. Such information is crucial to estimate the lower bound for the permanent electric dipole moments in the $X^1\Sigma^+$ and $H^1\Delta_1$ electronic states of ThO. Recently, Heaven and coworkers[75,77] designated the ThS molecule as the new and potentially good candidate for the eEDM. Their preliminary *ab initio* calculations confirm experimental findings.[75] This motivates us to carefully examine the electronic structures of both ThO and ThS using state-of-the-art relativistic coupled cluster methods. We would like to stress that our goal of the work presented in **[H1]** is not a direct determination of the lower bound for eEDM, but an in-depth examination of the electronic structures of ThO and ThS by pointing out similarities and differences between them.

Since the number of electrons in our systems is large, we have to find some compromise and correlate the chemically most important electrons. ThO and ThS ground state spectroscopic parameters calculated from the CCSD and CCSD(T) methods and various number of correlated electrons are reported in Table 4. It is evident from Table 4 that for ThO it is sufficient to correlate only 34 electrons ($5p$, $5d$, $6s$, $6p$, and $7s$ spinors of thorium as well as $2s$ and $2p$ spinors of oxygen) as a larger number of correlated electrons does not effect spectroscopic constants.

For the ThS molecule, the optimal number of correlated electrons seems to be 34 as

Table 4: The influence of correlated number of electrons (N_{corr}) on the ground state bond lengths (r_e), vibrational frequencies (ω_e), and force constants (f) of ThO and ThS using the dyall.v3z basis set for all elements.

	Method	N_{corr}	r_e [Å]	ω_e [cm^{-1}]	f [N/m]
ThO	CCSD	28	1.838	921	748.6
	CCSD	34	1.837	922	749.6
	CCSD	50	1.837	922	749.3
	CCSD(T)	28	1.848	894	704.0
	CCSD(T)	34	1.848	894	705.3
	CCSD(T)	50	1.848	894	705.1
ThS	CCSD	28	2.348	496	407.3
	CCSD	34	2.348	496	407.1
	CCSD	44	2.347	496	407.9
	CCSD	58	2.347	496	408.0
	CCSD(T)	28	2.357	482	384.4
	CCSD(T)	34	2.356	482	384.0
	CCSD(T)	44	2.355	482	385.1
	CCSD(T)	58	2.355	483	385.1

Paweł Tecmer

correlating additional electrons does not effect spectroscopic parameters considerably. The spinors of these calculations have similar atomic composition as the set of ThO with the same number of electrons, with the only difference that the thorium $5p$ spinors are substituted by the presence of sulfur $2p$ atomic spinors. It is worth notifying that the presence of thorium $4f$ atomic spinors in correlated calculations does not affect the spectroscopic constants of ThO and ThS. Hence, in all other calculations presented in **[H1]**, we correlated 34 electrons (32 for doubly charged molecules, *vide infra*) in the coupled cluster approach.

In Table 5, we analyzed the influence of basis set size on the ground state spectroscopic constants of ThO and ThS. It is evident from these results that the triple zeta quality basis set provides already very good results for both molecules. Comparing triple zeta results with those extrapolated to the basis set limit shows only minor differences in spectroscopic constants (see Table 5). Exception is the ThS equilibrium bond length, which changes up to 0.011 Å for both CCSD and CCSD(T).

In Table 6, we compare the new ground state theoretical results for ThO to the existing experimental and theoretical data available in the literature. One can see that our CCSD and CCSD(T) results are very close to experiment, outperforming the standard CASSCF/MRCI and CASPT2 approaches. Extrapolation to the basis set limit brings the CCSD(T) bond length (1.842 Å) closer to the experimental value of 1.840 Å. Both CCSD vibrational frequencies overestimate the experimental value by approximately 30 cm^{-1}. The triples correction on top of CCSD brings the characteristic vibrations very close to experimentally determined values (879–896

Table 5: The influence of the basis set size on the ground state bond lengths (r_e), vibrational frequencies (ω_e), and force constants (f) of ThO and ThS correlating 34 electrons.

	Method	Basis Th/{O,S}	r_e [Å]	ω_e [cm^{-1}]	f [N/m]
ThO	CCSD	dyall.v3z/dyall.v3z	1.837	922	749.6
	CCSD	dyall.v3z/cc-pVTZ	1.837	924	752.2
	CCSD	dyall.v4z/cc-pVQZ	1.833	924	752.7
	CCSD	CBS	1.831	924	753.3
	CCSD(T)	dyall.v3z/dyall.v3z	1.848	894	705.3
	CCSD(T)	dyall.v3z/cc-pVTZ	1.848	896	708.4
	CCSD(T)	dyall.v4z/cc-pVQZ	1.844	896	708.0
	CCSD(T)	CBS	1.842	896	707.8
ThS	CCSD	dyall.v3z/dyall.v3z	2.348	496	407.1
	CCSD	dyall.v3z/cc-pVTZ	2.348	497	409.3
	CCSD	dyall.v4z/cc-pVQZ	2.341	499	412.8
	CCSD	CBS	2.337	501	415.9
	CCSD(T)	dyall.v3z/dyall.v3z	2.356	482	384.0
	CCSD(T)	dyall.v3z/cc-pVTZ	2.356	483	386.5
	CCSD(T)	dyall.v4z/cc-pVQZ	2.349	486	390.4
	CCSD(T)	CBS	2.345	488	393.6

Paweł Tecmer

cm^{-1}).
Table 7 collects the ground state bond lengths and vibrational frequencies for ThS. Our CCSD and CCSD(T) vibrational frequencies are in very good agreement with the experimental values, with CCSD(T) being somehow closer. Specifically, the CCSD(T) values of 483 and 488 cm^{-1} fit quite well the experimental values of 475 and 479 cm^{-1}. Comparing the ground-state spectroscopic constants of ThO and ThS, we can see that the Th–S bond length is ca. 0.51 Å longer than the corresponding Th–O bond. Such a considerable difference can be explained by the approximately two times larger atomic sphere of sulfur. The force constants of ThO are roughly twice the value of ThS (705 vs. 385 N/m), thus the strength of the Th–O bond is approximately twice the strength of Th–S.
Table 8 lists the low-lying part of the adiabatic spectrum of the ThO molecule. The calculated excitation energies of ThO are mainly dominated by electron transfer from the occupied $7s$ spinor to the unoccupied $6d$ and $7p$ spinors of thorium. The composition of virtual spinors changes, however, with the bond distance. In general, the electronic spectrum of ThO can be divided into three blocks. The first block of the electronic spectrum covers excitations to the $6d$ spinors in the range of 5 000–8 500 cm^{-1}. Our Mulliken-based population analysis of virtual spinors confirms the leading contribution form the δ-type spinors in this part of the spectrum. In this region, the bond lengths are elongated by about 0.01–0.02 Å and vibrational frequencies lowered by approximately 40 cm^{-1} with respect to the ground state reference. The second block ranges from 10 000 to 13 000 cm^{-1} and includes electron transfer to $7p$ spinors. All equilibrium bond lengths for these excited states are slightly longer than in the first block of the ThO spectrum (see Table 8). The third block contains all the remaining excitations up to 18 000 cm^{-1} and covers electronic transitions to the mixed

Table 6: Equilibrium bond lengths (r_e) and vibrational frequencies (ω_e) of the $^1\Sigma^+$ ground-state ThO.

Method	r_e [Å]	ω_e[cm^{-1}]
Experimental		
PFI-ZEKE (gas phase)[78]	1.840	
MW (gas phase)[79]	1.840	
Electron Spec. (gas phase) [80]		896
IR Ne matrix[81]		887
IR Ar matrix[82]		879
Theoretical		
DFT/B3PW91[78]	1.846	898
CASSCF/MRCI [83]	1.862	867
Spin Orbit CASPT2[84]	1.862	856
Spin Free CASPT2[85]	1.861	879
Present work		
CCSD/dyall.v3z	1.837	922
CCSD/CBS	1.831	924
CCSD(T)/dyall.v3z	1.848	894
CCSD(T)/CBS	1.842	896

Paweł Tecmer

Table 7: Equilibrium bond lengths (r_e) and vibrational frequencies (ω_e) of the $^1\Sigma^+$ ground-state ThS.

Method	r_e[Å]	ω_e[cm^{-1}]
Experimental		
IR [86]		475
Electron Spec. (gas phase) [87]		479(1)
Theoretical		
B3LYP [88]	2.349	481
B3PW91 [86]	2.341	479
CASSCF/MRCI [87]	2.363	477
Present work		
CCSD/dyall.v3z	2.348	496
CCSD/CBS	2.337	501
CCSD(T)/dyall.v3z	2.356	482
CCSD(T)/CBS	2.345	488

6*d* and 7*p* molecular spinors. In this part of the spectrum, we see a lot of distortions in the bond lengths and the values of vibrational frequencies depending on the theoretical method used. In general, the IHFSCC(1,1) excitation energies are too low and the IHFSCC(0,2) excitation energies too high compared with experimental values. Comparing our IHFSCC(1,1) and IHFSCC(0,2) spectroscopic constants we see that both methods give similar results. The agreement between these two approaches is smallest in the lower part of the ThO spectrum and increases towards higher lying excited states. Both methods predict the same order of excites states, while the differences in excitation energies usually do not exceed 1 000 cm^{-1}. All FSCC spectroscopic parameters agree rather well with experimental data listed in Table 8. Specifically, the differences do not exceed 50 cm^{-1} in vibrational frequencies and 0.005 Å in bond lengths. Based on our analysis of the ground state spectroscopic

Table 8: Spin–orbit electronic spectrum of the ThO molecule. Adiabatic excitation energies, T_e (in cm^{-1}), bond lengths, r_e (in Å), and vibrational frequencies, ω_e (in cm^{-1}).

State	IHFSCC(1,1)			IHFSCC(0,2)			SO-CASPT2 [84]			Experiment		
Ω	T_e[cm^{-1}]	r_e[Å]	ω_e[cm^{-1}]	T_e[cm^{-1}]	r_e[Å]	ω_e[cm^{-1}]	T_e[cm^{-1}]	r_e[Å]	ω_e[cm^{-1}]	T_e[cm^{-1}]	r_e[Å]	ω_e[cm^{-1}]
0^+(X)	0	1.837	922	0	1.841	922	0	1.866	856	0	1.840	896
1 (H)	5 168	1.854	885	6 017	1.855	885	5 549	1.882	823	5 317	1.858	857
2 (Q)	6 086	1.853	886	6 866	1.854	886	6 693	1.880	828	6 128	1.856	858
3 (W)	7 694	1.852	887	8 438	1.852	889	8 408	1.878	835	8 600	-	-
0^-	10 701	1.861	857	10 911	1.857	882	10 370	1.901	784	-	-	-
0^+(A)	11 699	1.862	910	11 292	1.857	882	10 388	1.902	783	10 601	1.867	846
1 (B)				12 056	1.859	879	11 181	1.905	776	11 129	1.864	843
2	12 803	1.849	885	12 732	1.852	886	12 891	1.900	774	-	-	-
1 (C)	14 451	1.866	859	16 188	1.864	869	14 112	1.914	779	14 490	1.870	825
2	14 997	1.859	872	14 533	1.857	883	14 640	1.872	853	-	-	-
1 (D)	-	-	-	17 644	1.862	874	19 813	1.914	701	15 946	1.866	839
0^-	16 982	1.888	822	18 016	1.868	855	20 188	1.879	866	-	-	-
0^+(E)	14 370	1.868	855	17 280	1.859	875	17 912	1.902	781	16 320	1.867	829
2 (G)	-	-	-	-	-	-	17 339	1.920	759	18 010	1.882	809

Paweł Tecmer

constants one might expect that to a large extent these discrepancies are caused by the lack of triple excitations in our model (*vide supra* discussion on the CCSD and CCSD(T) results).

The adiabatic excitation energies of the ThS molecule are listed in Table 9. Similar to ThO, also the ThS electronic spectrum can be divided into three characteristic blocks. The lowest part of the spectrum covers excitations from the $7s$ atomic spinor to the $6d$ spinors in the range of 2 500–8 000 cm^{-1}. Despite the fact that excitation energies have similar character and the same symmetry, they are lower in energy by approximately 2 000 cm^{-1} than in the corresponding ThO molecule. Similar as in ThO, the optimal bond lengths for excited states are elongated by approximately 0.02 Å and vibrational frequencies lowered by about 20 cm^{-1} with respect to the ground state reference. In the second part of ThS spectrum covering excitations within 8 500 and 12 000 cm^{-1}, the bond lengths are elongated by additional 0.02 Å. In the ThS molecule, the separation between the first pair of 0^+ and 0^- states is lowered down to 400 cm^{-1} compared with 1 000 cm^{-1} in the ThO molecule. The remaining part of the ThS excitation energies is included in the third part of the spectrum. As in ThO, also here we observe a stronger sensitivity of the applied IHFSCC variant on the bond lengths and vibrational frequencies of excited states. The overall agreement between electronic spectra obtained from sector (1,1) and sector (0,2) of the Fock space is a little bit less satisfactory than for ThO. The largest difference between these two variants of the IHFSCC approach occurs in the lowest-lying part of the electronic spectrum and amounts to 2 000 cm^{-1} (cf. Table 9). This is very surprising as in this part of the electronic spectrum wave function compositions of the IHFSCC(1,1) and IHFSCC(0,2) model spaces are almost identical. Thus, orbital relaxation effects seem to be more important for ThS^{2+} than than for ThO^{2+}.

The analysis presented in **[H1]** suggest that the application of the IHFSCC(0,2) method for ionically bonded molecules such as ThO and ThS should give qualitatively correct and complete electronic spectra. This is particularly important for cases where

Table 9: Spin–orbit electronic spectrum of the ThS molecule. Adiabatic excitation energies, T_e (in cm^{-1}), bond lengths, r_e (in Å), and vibrational frequencies, ω_e (in cm^{-1}).

State	IHFSCC(1,1)			IHFSCC(0,2)			SO-MRCI[87]		
Ω	$T_e[cm^{-1}]$	r_e[Å]	$\omega_e[cm^{-1}]$	$T_e[cm^{-1}]$	r_e[Å]	$\omega_e[cm^{-1}]$	$T_e[cm^{-1}]$	r_e[Å]	$\omega_e[cm^{-1}]$
0	0	2.348	497	0	2.344	506	0	2.363	477
1	2 616	2.377	475	4 624	2.367	492	3 940	2.394	454
2	3 642	2.376	475	5 572	2.366	493	4 856	2.393	453
3	5 344	2.374	478	7 197	2.364	495	5 811	2.391	455
0^-	8 742	2.400	452	9 961	2.374	483	-	-	-
0^+	9 108	2.403	448	10 291	2.374	483	-	-	-
1	-	-	-	10 964	2.377	478	-	-	-
2	11 145	2.390	437	12 245	2.369	486	-	-	-
2	12 723	2.395	484	13 852	2.375	481	-	-	-
1	-	-	-	14 696	2.386	464	-	-	-
0^+	16 090	2.413	450	15 655	2.391	455	-	-	-
0^-	18 218	2.427	444	16 675	2.389	460	-	-	-

Paweł Tecmer

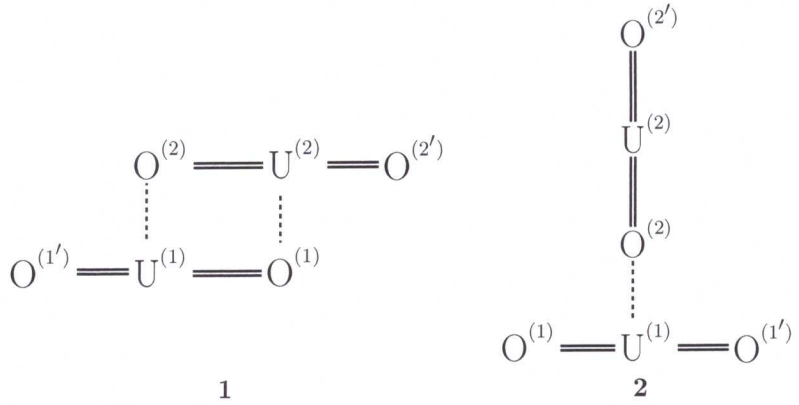

1 2

Figure 15: Lewis structures of the diamond (**1**) and T-shaped (**2**) clusters formed by two interacting uranyls.

the IHFSCC(1,1) electronic spectra could not be converged.

c.6 Towards reliable modeling of large actinide species.

As mentioned before, the $[UO_2]^{2+}$ molecule, commonly known as uranyl(VI), is the most stable and prevalent actinide oxide and usually constitutes the main component of larger uranium-containing complexes.[64,89] The $[UO_2]^{2+}$ building block features short U–O bond lengths (ca. 1.78 Å), a linear geometry ($\measuredangle$ (O–U–O) = 180°), and unique U–O symmetric and asymmetric vibrational frequencies. Since the symmetric stretching frequency ν_1 (Σ_g^+) in uranyl(VI) is IR-forbidden, in asymmetric surroundings it has a weak absorption signal in the range of 800 to 900 cm^{-1}. The asymmetric stretching frequency ν_3 (Σ_u^+), on the other hand, is IR-allowed and typically experimentally observable in the range of 900 to 1050 cm^{-1}. The asymmetric ν_3 stretching frequency is commonly used to identify the uranyl(VI) unit in larger uranium-containing compounds.[90–94] Furthermore, uranyl(VI) features a distinctive

Table 10: BP86 optimized structural parameters of diamond shaped CCI clusters. Bond lengths are given in Å and angles in degrees (°). The $d_{U^{(1)}\text{-}O^{(1')}}$ and $d_{U^{(1)}\text{-}O^{(1')}}$ bond lengths are equal to $d_{U^{(2)}\text{-}O^{(2')}}$ and $d_{U^{(2)}\text{-}O^{(2')}}$, respectively.

Compound	$d_{U^{(1)}\text{-}O^{(1)}}$	$d_{U^{(1)}\text{-}O^{(1')}}$	$d_{U^{(1)}\text{-}U^{(2)}}$	$d_{U^{(1)}\text{-}O^{(2)}}$	$\measuredangle_{O^{(1)}\text{-}U^{(1)}\text{-}O^{(1')}}$
$[(UO_2)_2]^{4+}_{[M=1]}$	1.81	1.72	3.47	2.38	179.2
$[(UO_2)_2]^{4+}_{[M=3]}$	1.81	1.75	3.69	2.55	171.8
$[(UO_2)_2]^{4+}_{[M=5]}$	1.85	1.78	3.50	2.41	178.5
$[(UO_2)_2]^{3+}_{[M=2]}$	1.85	1.74	3.40	2.33	178.6
$[(UO_2)_2]^{3+}_{[M=4]}$	1.86	1.79	3.58	2.44	172.7
$[(UO_2)_2]^{2+}_{[M=1]}$	1.91	1.78	3.32	2.27	177.7
$[(UO_2)_2]^{2+}_{[M=3]}$	1.92	1.79	3.38	2.28	179.9
$[(UO_2)_2]^{2+}_{[M=5]}$	1.96	1.82	3.35	2.26	176.6

Paweł Tecmer

Table 11: BP86 optimized structural parameters of T-shaped CCI clusters. Bond lengths are given in Å and angles in degrees (°). The $d_{U^{(1)}\text{-}O^{(1)}}$ and $d_{U^{(1)}\text{-}O^{(1')}}$ bonds are equivalent in all clusters

Compound	$d_{U^{(1)}\text{-}O^{(1)}}$	$d_{U^{(2)}\text{-}O^{(2)}}$	$d_{U^{(2)}\text{-}O^{(2')}}$	$d_{U^{(1)}\text{-}O^{(2)}}$	$\angle_{O^{(1)}\text{-}U^{(1)}\text{-}O^{(1')}}$
$[(UO_2)_2]^{4+}_{[M=1]}$	1.73	1.77	1.71	2.49	177.0
$[(UO_2)_2]^{4+}_{[M=3]}$	1.73	1.81	1.78	2.44	177.6
$[(UO_2)_2]^{4+}_{[M=5]}$	1.77	1.83	1.79	2.37	179.2
$[(UO_2)_2]^{3+}_{[M=2]}$	1.75	1.86	1.75	2.28	179.1
$[(UO_2)_2]^{3+}_{[M=4]}$	1.79	1.90	1.75	2.22	176.1
$[(UO_2)_2]^{2+}_{[M=1]}$	1.79	1.87	1.78	2.30	177.7
$[(UO_2)_2]^{2+}_{[M=3]}$	1.79	1.87	1.78	2.32	178.1
$[(UO_2)_2]^{2+}_{[M=5]}$	1.80	1.91	1.86	2.32	177.0

Table 12: Stability of the diamond and T-shaped structures in kcal/mol (calculated with PBE0 and the scalar ZORA Hamiltonian). The relative energies of the compounds with a total charge of 4+, 3+, and 2+ are adjusted to the most stable one within each charge group.

Compound	Diamond	T-shape
$[(UO_2)_2]^{4+}_{[M=1]}$	20.5	0.0
$[(UO_2)_2]^{4+}_{[M=3]}$	100.6	57.5
$[(UO_2)_2]^{4+}_{[M=5]}$	168.4	117.6
$[(UO_2)_2]^{3+}_{[M=2]}$	21.0	0.0
$[(UO_2)_2]^{3+}_{[M=4]}$	111.4	57.4
$[(UO_2)_2]^{2+}_{[M=1]}$	39.2	48.4
$[(UO_2)_2]^{2+}_{[M=3]}$	27.6	0.0
$[(UO_2)_2]^{2+}_{[M=5]}$	60.4	88.0

electron absorption spectrum ($\sigma \rightarrow \phi$ and $\sigma \rightarrow \delta$) in the range of 2.2 to 3.2 eV (400–550 nm).[28,63]

Despite its unique characteristics, experimental identification of the $[UO_2]^{2+}$ unit is often hampered by the coordination of another uranyl "yl" oxygen to the actinyl centre.[95] Such interactions are commonly referred to as cation–cation interactions (CCIs).[96–98] The CCIs might induce an irregular elongation of the U–O bonds and asymmetry in the IR or Raman spectra.[99–101] Moreover, the CCIs between the $[UO_2]^{2+}$ fragments can be further grouped into two distinct categories: diamond and T-shape (cf. **1** and **2** in Figure 15). CCIs are, however, not limited to $[UO_2]^{2+}$ fragments. A series of so-called "mixed-valent" $[UO_2]^{2+} \cdots [UO_2]^{+}$ compounds as well as $[UO_2]^{+} \cdots [UO_2]^{+}$ assemblies have been identified experimentally.[102]

Reduction of $[UO_2]^{2+}$ to $[UO_2]^{+}$ promotes the formation of CCIs as a result of the higher Lewis basicity of the "yl" oxygen atoms in the $[UO_2]^{+}$ cation. The presence

Paweł Tecmer

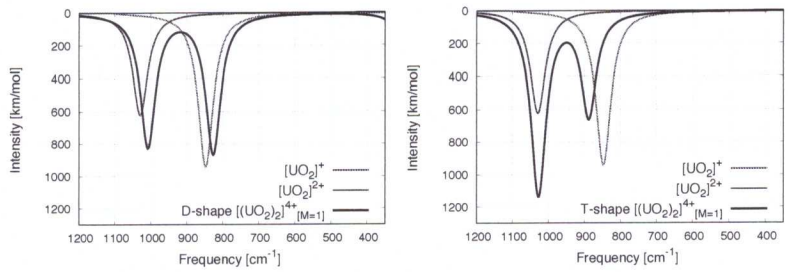

(a) Diamond (left) and T-shape (right) $[(UO_2)_2]^{4+}_{[M=1]}$

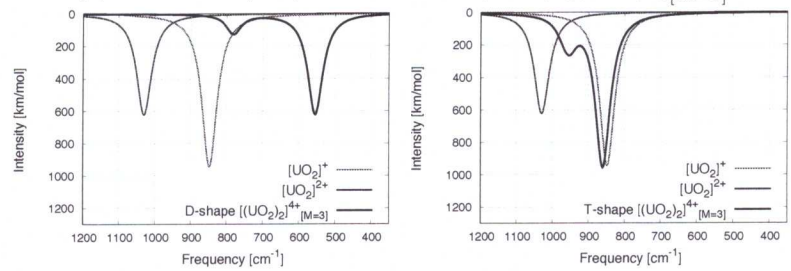

(b) Diamond (left) and T-shape (right) $[(UO_2)_2]^{4+}_{[M=3]}$

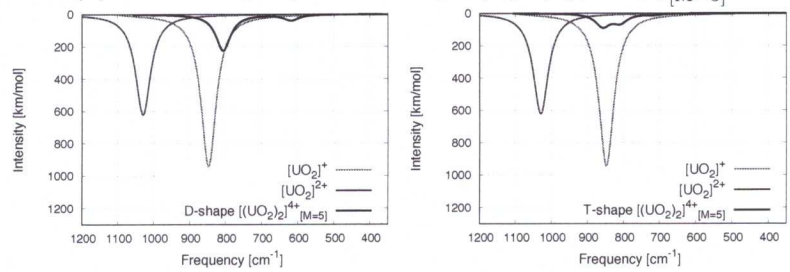

(c) Diamond (left) and T-shape (right) $[(UO_2)_2]^{4+}_{[M=5]}$

Figure 16: BP86 vibrational spectra of $[(UO_2)_2]^{4+}$ compared to the bare $[UO_2]^{2+}$ and $[UO_2]^+$ species.

of an additional electron in the $[UO_2]^+$ system, which is located on the non-bonding uranium $5f_\delta$ or $5f_\phi$ orbital, leads to weakening and elongation of the U–O bonds. This results in a red shift of the ν_1 and ν_3 vibrational frequencies. Due to a singly-occupied f-orbital, the electronic spectrum of $[UO_2]^+$ features the characteristic f–f transitions in the range of 0.5 to 3.7 eV (330–2500 nm).[103]
In general, CCIs may trigger disproportionation reactions of $[UO_2]^+$ to $[UO_2]^{2+}$ and U^{4+}, making the isolation of a specific class of actinyl ions particularly challenging. Thus, a better understanding of the chemistry in CCIs and of the bonding situation between different uranyl fragments is of crucial importance in nuclear chemistry. While there is abundant experimental data for CCIs between uranyl cations,[99–101] their existence could not be confirmed by theoretical approaches. The only existing quantum chemical study related to this topic has been conducted by McKee and Swart[104] and indicated that the $[UO_2]^{2+} \cdots [UO_2]^{2+}$ assemblies are not stable, neither in the gas phase nor in solution, due to the strong electrostatic repulsion between uranyl cations. To bridge the gap between theory and experiment and to dissect

Paweł Tecmer

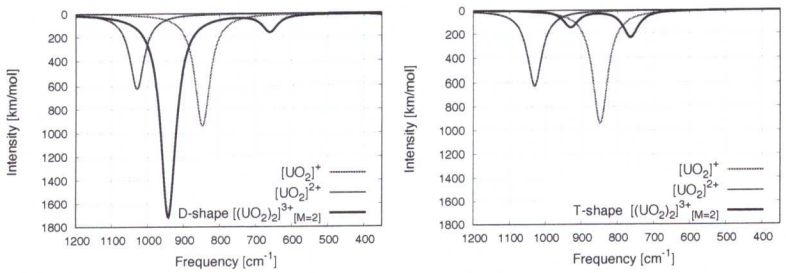

(a) Diamond (left) and T-shape (right) $[(UO_2)_2]^{3+}_{[M=2]}$

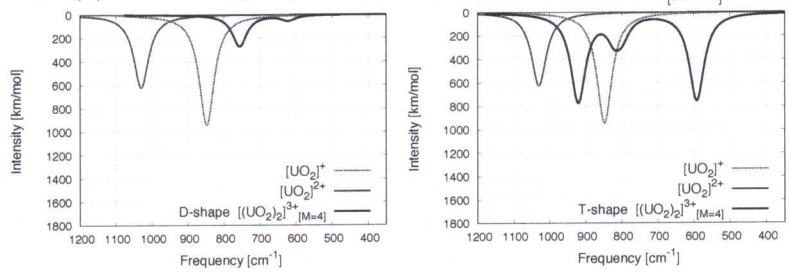

(b) Diamond (left) and T-shape (right) $[(UO_2)_2]^{3+}_{[M=4]}$

Figure 17: BP86 vibrational spectra of $[(UO_2)_2]^{3+}$ compared to the bare $[UO_2]^{2+}$ and $[UO_2]^+$ species.

the nature of the CCIs, we investigate in **[H3]** a series of model systems for CCIs: $[UO_2]^{2+}\cdots[UO_2]^{2+}$ ($[(UO_2)_2]^{4+}$), $[UO_2]^{2+}\cdots[UO_2]^{+}$ ($[(UO_2)_2]^{3+}$), and $[UO_2]^{+}\cdots[UO_2]^{+}$ ($[(UO_2)_2]^{2+}$) using present-day state-of-the-art quantum chemistry methods. Our study demonstrates that all of these compounds indeed exist. Specifically in **[H3]**, we analyzed the supra-molecular structures, energetic stabilities, vibrational frequencies, and vertical excitation energies of the above mentioned uranyl assemblies in structural rearrangements **1** and **2** and different spin multiplicities.

It is well-known that the electronic structure of uranyl(VI) around the equilibrium geometry is reliably represented by a single Slater determinant. The situation is different in uranyl(V), where the $\sigma_u^2\phi_u$ and $\sigma_u^2\delta_u$ electronic configurations are quasi-degenerate.[28,105] Yet, single-reference methods such as DFT and coupled cluster can handle these types of quasi-degeneracies reasonably well, providing acceptably good results for uranyl(V) compounds.[103] Based on previous studies of uranyl and uranyl-containing compounds, we can assume that DFT also works reasonably well when the two uranyl units are weakly bound together forming the CCI cluster.

The influence of the CCI on geometries of the bare $[UO_2]^+$ and $[UO_2]^{2+}$ moieties is presented in Tables 10 and 11 for different charges and spin multiplicities (M) of the dications. For the dications in diamond shape, we observe that the two uranyl subunits have similar structural characteristics, where the terminal U–O bonds (indicated by ') are shorter than the interior ones. Furthermore, the differences between the terminal and interior U–O bond lengths in each CCI cluster are, in general, larger than the differences between the optimal U–O bond distances in uranyl(VI) and uranyl(V). If the number of unpaired electrons in the dications increases and the molecular charge simultaneously decreases, the U–O bonds elongate. No changes in

Paweł Tecmer

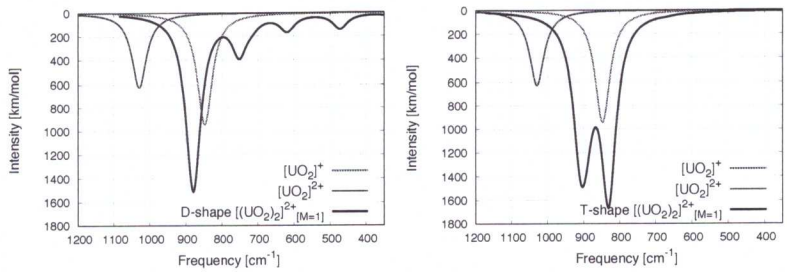

(a) Diamond (left) and T-shape (right) $[(UO_2)_2]^{2+}_{[M=1]}$

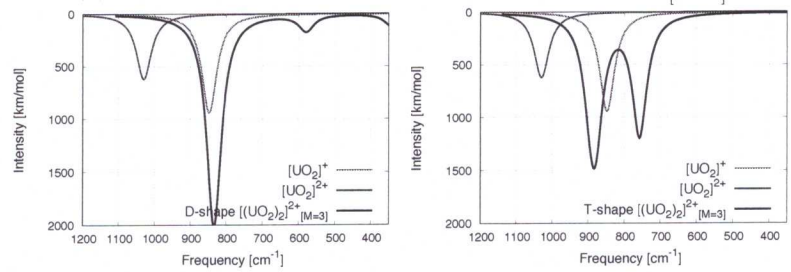

(b) Diamond (left) and T-shape (right) $[(UO_2)_2]^{2+}_{[M=3]}$

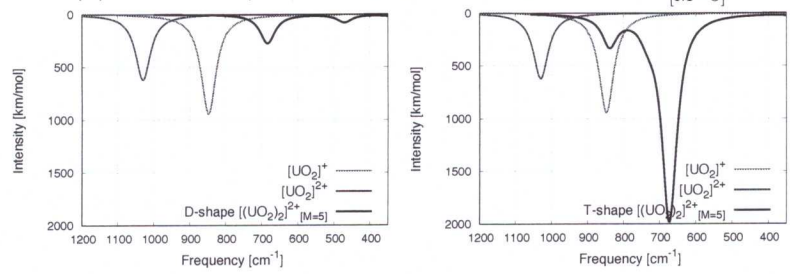

(c) Diamond (left) and T-shape (right) $[(UO_2)_2]^{2+}_{[M=5]}$

Figure 18: BP86 vibrational spectra of $[(UO_2)_2]^{2+}$ compared to the bare $[UO_2]^{2+}$ and $[UO_2]^+$ species.

the U–U non-bonding distances can be observed for the diamond-shaped structures. In most of the diamond-shaped CCI clusters, the uranyl units preserve a linear geometry with the exception of $[(UO_2)_2]^{4+}_{[M=3]}$ and $[(UO_2)_2]^{3+}_{[M=4]}$, where the distortion from linearity is greater than 5°.

The structural parameters of the T-shaped CCI clusters are summarized in Table 11. In these dications, one uranyl unit ($O^{(1)} - U^{(1)} - O^{(1')}$) has symmetric U–O bond lengths with a slightly distorted linearity (less than 5°), whereas the second uranyl unit ($O^{(2)} - U^{(2)} - O^{(2')}$) features asymmetric U–O bond distances, while fully preserving linearity.

From an energetical point of view, the most stable compounds are the T-shaped $[(UO_2)_2]^{4+}_{[M=1]}$, $[(UO_2)_2]^{3+}_{[M=2]}$, $[(UO_2)_2]^{2+}_{[M=3]}$ structures. These clusters are more than 20 kcal/mol lower in energy than the corresponding diamond structures with the same spin state and number of electrons. Furthermore, the T-shaped CCI compounds are generally more stable than the diamond-shaped assemblies of similar charge (see

Paweł Tecmer

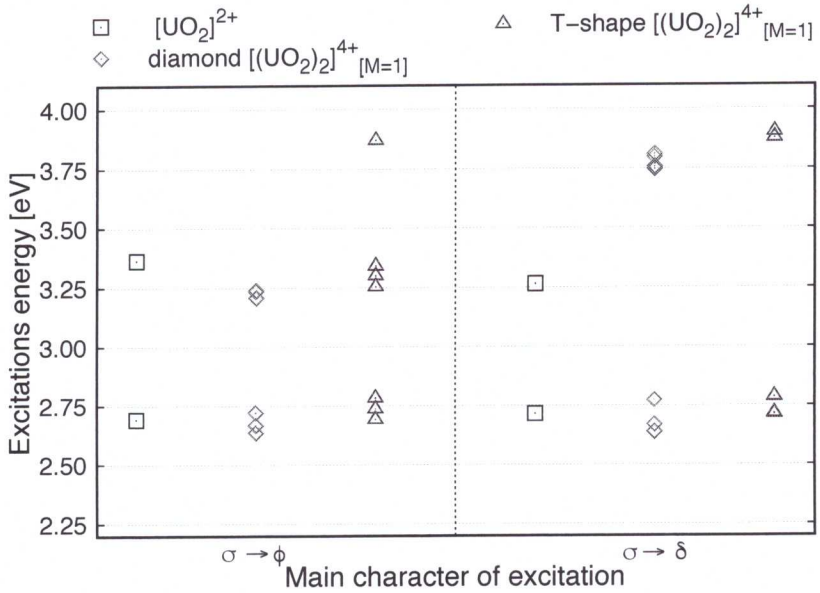

Figure 19: Vertical excitation energies of $[(UO_2)_2]^{4+}$ clusters.

Table 12). The only exceptions are the $[(UO_2)_2]^{2+}_{[M=1]}$ and $[(UO_2)_2]^{2+}_{[M=3]}$ molecules. Theoretical vibrational spectra of all CCI clusters in the range of 350 to 1200 cm^{-1} are presented in Figures 16–18. The most intensive peaks correspond to the original asymmetric (ν_3) stretching frequencies in each uranyl subunit. The structural asymmetries induced by the CCI on the U–O bond lengths in each uranyl subunit, however, significantly affect the positions and intensities of the characteristic $[UO_2]^{2+}$ vibrational stretching frequencies. Furthermore, almost none of the CCI spectra overlaps solely with the uranyl(VI) or uranyl(V) reference spectra. Thus, we can no longer identify the nature of the U–O bond or the oxidation state of each uranium atom in the majority of such dications solely based on vibrational spectra. The only exceptions are the diamond $[(UO_2)_2]^{2+}_{[M=1]/[M=3]}$ and T-shaped $[(UO_2)_2]^{4+}_{[M=3]}$ compounds, whose spectra have the same characteristic features as those of the bare $[UO_2]^{+}$ unit.

Electronic (UV-VIS) spectroscopy of uranyl ions represents another technique to probe the nature of the U–O bond. Comparing the electronic spectra of the investigated dications to the bare uranyl(VI) and uranyl(V) species, we observe that the characteristic features of the $[UO_2]^{2+}$ spectrum are only present for the compounds with a molecular charge of 4+, while the clusters with charge 2+ result in spectra that closely resemble the $[UO_2]^{+}$ spectrum. The $[(UO_2)_2]^{3+}_{[M=2]}$ clusters have features of both uranyl(VI) and uranyl(V) electronic spectra. The CCIs lift the degeneracy of the non-bonding δ and ϕ orbitals, which splits the characteristic $\sigma \rightarrow \delta$ and $\sigma \rightarrow \phi$ electronic transitions present in $[UO_2]^{2+}$ (see Figures 19–21). Furthermore, all excitation energies of the diamond-shaped $[(UO_2)_2]^{4+}_{[M=1]}$ and $[(UO_2)_2]^{2+}_{[M=3]}$ compounds lie below the $[UO_2]^{2+}$ and $[UO_2]^{+}$ electronic transitions, respectively. This is not the case for the T-shaped clusters.

While the $[(UO_2)_2]^{4+}_{[M=1]}$ clusters have a rather simple electronic spectrum, the elec-

Paweł Tecmer

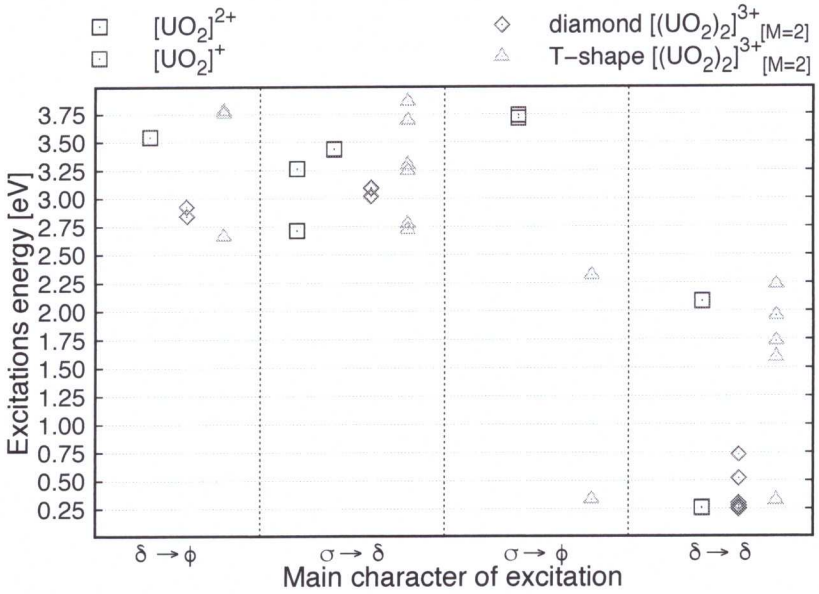

Figure 20: Vertical excitation energies of $[(UO_2)_2]^{3+}$ clusters.

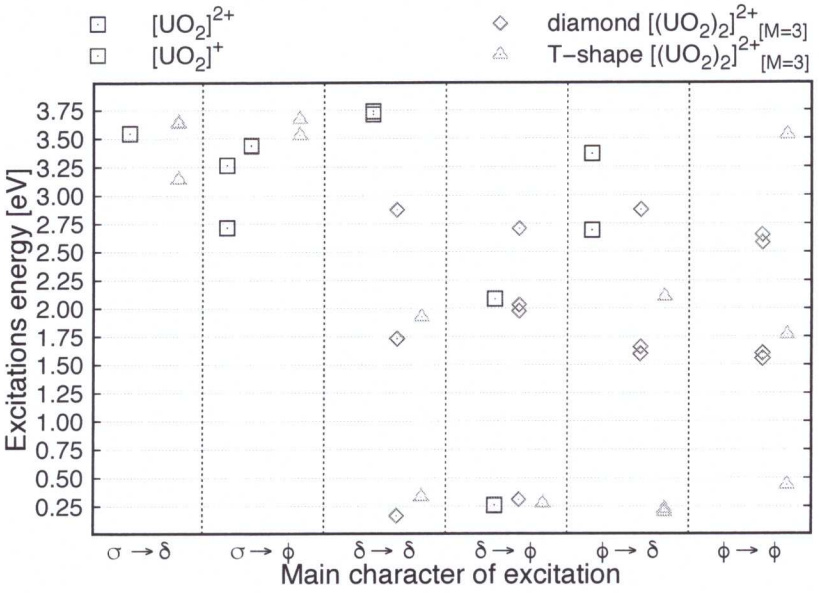

Figure 21: Vertical excitation energies of $[(UO_2)_2]^{2+}$ clusters.

tronic spectra of the $[(UO_2)_2]^{3+}_{[M=2]}$ and $[(UO_2)_2]^{2+}_{[M=3]}$ clusters are much more complex. Specifically, all the (lowest-lying) electronic transitions occur from the partially occupied ϕ or δ orbitals to one of the σ, δ or ϕ orbitals. While electrons are excited from the δ and σ orbitals in the bare uranyl(V) compound, the electronic transitions observed in the $[(UO_2)_2]^{3+}_{[M=2]}$ and $[(UO_2)_2]^{2+}_{[M=3]}$ assemblies also originate from the ϕ orbital. Nevertheless, the characteristic f–f transitions in the range of 0.1 to 1.0 eV confirm the presence of the uranyl(V) unit in the investigated dications.

Paweł Tecmer

(d) Summary and impact of research

The presented series of papers (**[H1]**–**[H10]**) describes the development and application of modern electronic structure theories to both model and understand complex electronic structures of heavy elements. The applicant has demonstrated the superiority of quantum entanglement- and correlation-based measures such as the single-orbital entropy and the mutual information over standard approaches to elucidate electron correlation effects **[H9]**–**[H10]**, bonding patters **[H7]**–**[H9]**, and complexation **[H8]**, as well as in choosing optimal active spaces **[H2]** and monitoring reaction pathways **[H4]**–**[H5]**. These concepts originating from quantum information theory have paved the way towards a better understanding of complex electronic structures and the reliability of different quantum chemistry methods. The entanglement- and correlation-based measures can be obtained from the elements of the one-, two-, three-, and four-particle reduced density matrices of any electron correlation method and can be thus applied to validate any new approximate electron correlation theory. In practical applications, these quantities can be efficiently calculated from modern electronic structure methods such as the DMRG algorithm and AP1roG. An analysis based on the single-orbital entropy and (orbital-pair) mutual information combined with modern electronic structure methods are particularly instructive in modeling electronic structures of actinide species as demonstrated in **[H2]**, **[H4]**, and **[H8]**. Since it is difficult to choose *ad hoc* the most important, that is, strongly-correlated orbitals in actinide compounds and hence an adequate quantum chemistry method, the methodology demonstrated by the applicant is of great importance not only to actinide-related research, but also to theoretical physics as well as general, organic, and bio-organic chemistry.

Besides electron correlation, it is important to account for relativistic effects in heavy element compounds. While it is well-understood how to include scalar relativistic effects, there are still many ways to choose to account for spin–orbit coupling. Most importantly, their performance has not been scrutinize in the literature. This is particularly true for the heaviest elements as actinides. The applicant investigated the performance of various two-electron approximations to the spin–orbit coupling in **[H8]**. Specifically, it has been shown that the molecular mean field approach in the X2C Hamiltonian gives spin–orbit splittings that are almost identical to those obtained from the more expensive four-component Dirac–Coulomb Hamiltonian for a series of actinide species. This means that electronic spectra of actinides can be calculated within a two-component methodology without any significant loss of accuracy, but at substantially lower cost **[H8]**.

Furthermore, the applicant combined the acquired knowledge on electron correlation and relativistic effects as well as on the reliability of different quantum chemistry methods to bridge the gap between theory and experiment for actinide chemistry in **[H1]** and **[H3]**. Thus, the series of publications presented in **[H1]**–**[H10]** opens the way to study larger and, most importantly, realistic molecular species, for which experimental manipulations are very limited.

Paweł Tecmer

5 Discussion of other scientific achievements, after PhD studies

Apart from the publications discussed above, the applicant's remaining scientific research activity (after obtaining his PhD diploma) mainly focused on the development of new electronic structure methods based on the AP1roG wave function. Specifically, in **[P9]** a variational orbital optimization protocol (voo) for AP1roG was developed and tested for the one-dimensional Hubbard model and the quantum chemical Hamiltonian. More rigorous assessment of the voo-AP1roG model for modeling potential energy surfaces and predicting spectroscopic constants was presented in **[P7]**. In a follow up work (**[P8]**), a new orbital optimization scheme based on the seniority number was developed, resulting in the PS2-AP1roG approach. Further extensions to this nonvariational orbital optimization protocol were introduced and tested in **[P6]**. The elements of the one- and two-particle reduced density matrices needed to calculate the single-orbital entropy and mutual information from AP1roG were derived in **[P5]**. The quantum entanglement analysis was further used to analyze the electron correlation effects from AP1roG in hydrogen rings, chains, and the Hubbard model in **[P2]**. Finally, in **[P1]** a series of perturbation energy corrections on top of AP1roG was developed, implemented, and tested to account for the missing part of the dynamic energy within AP1roG.

Besides, the applicant closely collaborates with the experimental molecular physics group at NCU in Torun focusing on modeling electronic structures and properties of cold molecules. Some preliminary results were published in **[P10]**, where highly accurate theoretical data was used to model the short range part of the RbYb potential.

In **[P4]**, the work on the interaction of metal with olefines presented in **[H5]** using the quantum entanglement analysis has been extended to heavier elements and bisethene ligands. This work is not part of the habilitation thesis due to lacking contact with the first author.

In addition, in **[P3]** the quality and accuracy of DFT in predicting magnetization densities obtained from various approximate exchange–correlation functionals was assessed by comparing them to CASSCF reference distributions.

Finally, the applicant actively participates in the development of an open-source quantum chemistry software package called PIERNIK, developed by scientists at NCU Torun. The applicant's contributions include the module on relativistic effective core potentials, the general framework, and code maintenance. A first release of the code is planned for the end of 2019.

5.1 List of publications not included in section 4, after PhD studies

[P1] K. Boguslawski, **P. Tecmer**, *"Benchmark of dynamic electron correlation models for seniority-zero wave functions and their application to thermochemistry"*, *J. Chem. Theory Comput.* 13 **2017**, 5966-5983.

[P2] K. Boguslawski, **P. Tecmer**, Ö. Legeza, *"Analysis of two-orbital correlations*

Paweł Tecmer

in wave functions restricted to electron-pair states", Phys. Rev. B 94 **2016**, 155126.

[P3] D. Stuart, **P. Tecmer**, P. W. Ayers, K. Boguslawski, *The Effect of Nitrido, Azide, and Nitrosyl Ligands on Magnetization Densities and Magnetic Properties of Iridium PNP Pincer-Type Complexes, RSC Adv.* 5 **2015**, 84311-84320.

[P4] Y. Zhao, K. Boguslawski, **P. Tecmer**, C. Duperrouzel, G. Barcza, O. Legeza, P. W. Ayers, *Dissecting the bond formation process of d^{10}-metal-ethene complexes with multi-reference approaches, Theor. Chem. Acc.* 134 **2015**, 120 (**corresponding author**).

[P5] K. Boguslawski, **P. Tecmer**, *"Orbital entanglement in quantum chemistry", Int. J. Quantum Chem.* 115 **2015**, 1289-1295 (**invited article**); K. Boguslawski, **P. Tecmer**, *"Erratum: Orbital entanglement in quantum chemistry", Int. J. Quantum Chem.* 117 **2017**, e25455.

[P6] K. Boguslawski, **P. Tecmer**, P. W. Ayers, P. Bultinck, S. De Baerdemacker, D. Van Neck, *"Nonvariational orbital optimization techniques for the AP1roG wave function", J. Chem. Theory Comput.* 10 **2014**, 4873-4882.

[P7] **P. Tecmer**, K. Boguslawski, P. A. Johnson, P. A. Limacher, M. Chan, T. Verstraelen, P. W. Ayers, *"Assessing the accuracy of new geminal-based approaches", J. Phys. Chem. A* 118 **2014**, 9058-9068.

[P8] K. Boguslawski, **P. Tecmer**, P. A. Limacher, P. A. Johnson, P. W. Ayers, P. Bultinck, S. De Baerdemacker, D. Van Neck, *"Projected seniority-two orbital optimization of the antisymmetric product of one-reference orbital geminal", J. Chem. Phys.* 140 **2014**, 214114.

[P9] K. Boguslawski, **P. Tecmer**, P. W. Ayers, P. Bultinck, S. De Baerdemacker, D. Van Neck, *"Efficient description of strongly correlated electrons with mean-field cost", Phys. Rev. B* 89 **2014**, 201106(R).

[P10] M. Borkowski, Piotr S. Żuchowski, R. Ciuryło, P. S. Julienne, D. Kędziera, Ł. Mentel, **P. Tecmer**, F. Münchow, C. Bruni, and A. Görlitz, *"Scattering lengths in isotopologues of the RbYb system", Phys. Rev. A* 88 **2013**, 052708.

5.2 Bibliometric data (according to Web of Science)

(As of November 21, 2018)	
h-index:	14
number of citations:	491
(without self-citations)	(381)
number of published papers:	26

Paweł Tecmer

Bibliography

[1] E. Schrödinger, *Phys. Rev.*, 1926, **28**, 1049–1070.

[2] M. Born and J. R. Oppenheimer, *Ann. Phys.*, 1927, **84**, 457.

[3] P. A. M. Dirac, *Proc. Roy. Soc.*, 1928, **117**, 610–624.

[4] P. A. M. Dirac, *Proc. Roy. Soc.*, 1928, **118**, 351–361.

[5] P. A. M. Dirac, *Proc. Roy. Soc.*, 1930, **126**, 360–365.

[6] P. Schwerdtfeger, *Relativistic electronic structure theory. Part I. Fundamentals*, Elsevier, 2002.

[7] K. G. Dyall and J. K. Fægri, *Introduction to Relativistic Quantum Chemistry*, Oxford, 2007.

[8] M. Reiher and A. Wolf, *Relativistic Quantum Chemistry: the Fundamental Theory of Molecular Science*, John Wiley & Sons, 2014.

[9] J. Autschbach, *J. Chem. Phys.*, 2012, **136**, 150902.

[10] P. Pyykko, *Chem. Rev.*, 1988, **88**, 563.

[11] M. Dolg and X. Cao, *Chem. Rev.*, 2012, **112**, 403–480.

[12] M. Reiher and A. Wolf, *J. Chem. Phys.*, 2004, **121**, 2037–47.

[13] M. Reiher and A. Wolf, *J. Chem. Phys.*, 2004, **121**, 10945–56.

[14] M. Barysz, in *Theoretical chemistry and physics of heavy and superheavy elements*, Springer, 2003, pp. 349–397.

Paweł Tecmer

[15] P. Tecmer, K. Boguslawski and D. Kędziera, in *Handbook of computational chemistry*, ed. J. Leszczyński, Springer Netherlands, Dordrecht, 2017, vol. 2, pp. 885–926.

[16] P.-O. Löwdin, *Phys. Rev.*, 1955, **97**, 1509–1520.

[17] O. Sinanoğlu and D. F. Tuan, *J. Chem. Phys.*, 1963, **38**, 1740–1748.

[18] R. J. Bartlett and J. F. Stanton, *Rev. Comput. Chem.*, 1994, **5**, 65–169.

[19] R. J. Bartlett and M. Musiał, *Rev. Mod. Phys.*, 2007, **79**, 291–350.

[20] T. Helgaker, P. Jørgensen and J. Olsen, *Molecular Electronic-Structure Theory*, Wiley, Chichester, 2000.

[21] D. I. Lyakh, M. Musiał, V. F. Lotrich and . J. Bartlett, *Chem. Rev.*, 2012, **112**, 182–243.

[22] P. G. Szalay, T. Müller, G. Gidofalvi, H. Lischka and R. Shepard, *Chem. Rev.*, 2012, **112**, 108–181.

[23] T. J. Lee and P. R. Taylor, *Int. J. Quantum Chem.*, 1989, **23**, 199–207.

[24] T. J. Lee, J. E. Rice, G. E. Scuseria and H. F. Schaefer III, *Theor. Chim. Acta*, 1989, **75**, 81–98.

[25] M. L. Leininger, I. M. B. Nielsen, T. D. Crawford and C. L. Janssen, *Chem. Phys. Lett.*, 2000, **328**, 431–436.

[26] C. L. Janssen and I. M. B. Nielsen, *Chem. Phys. Lett.*, 1998, **290**, 423–430.

[27] W. Jiang, N. J. DeYonker and A. K. Wilson, *J. Chem. Theory Comput.*, 2012, **8**, 460–468.

[28] F. Réal, A. S. P. Gomes, L. Visscher, V. Vallet and E. Eliav, *J. Phys. Chem. A*, 2009, **113**, 12504–12511.

[29] P. Tecmer, A. S. P. Gomes, U. Ekström and L. Visscher, *Phys. Chem. Chem. Phys.*, 2011, **13**, 6249–6259.

[30] V. Vedral, *Rev. Mod. Phys.*, 2002, **74**, 197–233.

[31] P. Ziesche, *Int. J. Quantum Chem.*, 1995, **56**, 363–369.

[32] A. V. Luzanov and O. V. Prezhdo, *Int. J. Quantum Chem.*, 2005, **102**, 582–601.

[33] T. Juhász and D. A. Mazziotti, *J. Chem. Phys.*, 2006, **125**, 174105.

[34] A. V. Luzanov and O. Prezhdo, *Mol. Phys.*, 2007, **105**, 2879–2891.

[35] L. Greenman and D. A. Mazziotti, *J. Chem. Phys.*, 2010, **133**, 164110.

[36] S. R. White, *Phys. Rev. Lett.*, 1992, **69**, 2863–2866.

Paweł Tecmer

[37] S. R. White, *Phys. Rev. B*, 1993, **48**, 10345–10356.

[38] S. R. White and R. L. Martin, *J. Chem. Phys.*, 1999, **110**, 4127–4130.

[39] J. Rissler, R. M. Noack and S. R. White, *Chem. Phys.*, 2006, **323**, 519–531.

[40] Ö. Legeza and J. Sólyom, *Phys. Rev. B*, 2003, **68**, 195116.

[41] B. Groisman, S. Popescu and A. Winter, *Phys. Rev. A*, 2005, **72**, 032317.

[42] M. Wolf, F. Verstraete, M. Hastings and J. Cirac, *Phys. Rev. Lett.*, 2008, **100**, 070502.

[43] G. Barcza, R. Noack, J. Sólyom and Ö. Legeza, *Phys. Rev. B*, 2014, **92**, 125140.

[44] O. Legeza, R. M. Noack, J. Sólyom and L. Tincani, in *Computational Many-Particle Physics*, ed. H. Fehske, R. Schneider and A. Weiße, Springer, Berlin/Heidelerg, 2008, vol. 739 of Lect. Notes Phys., pp. 653–664.

[45] K. H. Marti and M. Reiher, *Z. Phys. Chem.*, 2010, **224**, 583–599.

[46] G. K.-L. Chan and S. Sharma, *Annu. Rev. Phys. Chem.*, 2011, **62**, 465–481.

[47] K. Boguslawski and P. Tecmer, *Int. J. Quantum Chem.*, 2015, **115**, 1289–1295.

[48] K. Boguslawski and P. Tecmer, *Int. J. Quantum Chem.*, 2017, **117**, e25455.

[49] K. Boguslawski, P. Tecmer, P. W. Ayers, P. Bultinck, S. De Baerdemacker and D. Van Neck, *Phys. Rev. B*, 2014, **89**, 201106(R).

[50] K. Boguslawski, P. Tecmer, P. A. Limacher, P. A. Johnson, P. W. Ayers, P. Bultinck, S. De Baerdemacker and D. Van Neck, *J. Chem. Phys.*, 2014, **140**, 214114.

[51] K. Boguslawski, P. Tecmer, P. W. Ayers, P. Bultinck, S. De Baerdemacker and D. Van Neck, *J. Chem. Theory Comput.*, 2014, **10**, 4873–4882.

[52] V. Murg, F. Verstraete, R. Schneider, P. R. Nagy and Ö. Legeza, *J. Chem. Theory Comput.*, 2015, **11**, 1027–1036.

[53] O. Legeza and J. Sólyom, *Phys. Rev. B*, 2004, **70**, 205118.

[54] P. Tecmer, K. Boguslawski, P. A. Limacher, P. A. Johnson, M. Chan, T. Verstraelen and P. W. Ayers, *J. Phys. Chem. A*, 2014, **118**, 9058–9068.

[55] K. Boguslawski, P. Tecmer, O. Legeza and M. Reiher, *J. Phys. Chem. Lett.*, 2012, **3**, 3129–3135.

[56] L. Maron, T. Leininger, B. Schimmelpfennig, V. Vallet, J.-L. Heully, C. Teichteil, O. Gropen and U. Wahlgren, *Chem. Phys.*, 1999, **244**, 195–201.

[57] A. Kovacs and R. J. M. Konings, *J. Phys. Chem. A*, 2012, **115**, 6646–6656.

[58] I. Infante, A. S. P. Gomes and L. Visscher, *J. Chem. Phys.*, 2006, **125**, 074301.

Paweł Tecmer

[59] G. L. Macchia, I. Infante, J. Raab, J. K. Gibson and L. Gagliardi, *Phys. Chem. Chem. Phys.*, 2008, **48**, 7278.

[60] P. Pyykkö, J. Li and N. Runeberg, *J. Phys. Chem.*, 1994, **98**, 4809–4813.

[61] L. Gagliardi and B. O. Roos, *Chem. Phys. Lett.*, 2000, **331**, 229.

[62] N. Kaltsoyannis, *Inorg. Chem.*, 2000, **39**, 6009–6017.

[63] S. Matsika, Z. Zhang, S. R. Brozell, J.-P. Blaudeau, Q. Wang and R. M. Pitzer, *J. Phys. Chem. A*, 2001, **105**, 3825–3828.

[64] R. G. Denning, *J. Phys. Chem. A*, 2007, **111**, 4125–4143.

[65] J. Li, B. E. Bursten, B. Liang and L. Andrews, *Science*, 2002, **295**, 2242–2245.

[66] I. Infante and L. Visscher, *J. Chem. Phys.*, 2004, **121**, 5783.

[67] T. Yang, R. Tyagi, Z. Zhang and R. M. Pitzer, *Mol. Phys.*, 2009, **107**, 1193–1195.

[68] P. Tecmer, H. van Lingen, A. S. P. Gomes and L. Visscher, *J. Chem. Phys.*, 2012, **137**, 084308.

[69] T. Fleig, *Chem. Phys.*, 2011, **395**, 2–15.

[70] P. S. Bagus, E. S. Ilton, R. L. Martin, H. J. A. Jensen and S. Knecht, *Chem. Phys. Lett.*, 2012, **546**, 58–62.

[71] M. Ilias and T. Saue, *J. Chem. Phys.*, 2007, **126**, 064102.

[72] B. A. Hess, C. M. Marian, U. Wahlgren and O. Gropen, *Chem. Phys. Lett.*, 1996, **251**, 365–371.

[73] J. Sikkema, L. Visscher, T. Saue and M. Ilias, *J. Chem. Phys.*, 2009, **131**, 124116.

[74] J. A. Gaunt, *Proc. R. Soc. Lon.*, 1929, **A122**, 513.

[75] M. C. Heaven, B. J. Barker and I. O. Antonov, *Phys. Rev. A*, 2014, **118**, 10867–10881.

[76] T. A. C. J. Baron, W. C. Campbell, D. DeMille, J. M. Doyle, G. Gabrielse, Y. V. Gurevich, P. W. Hess, N. R. Hutzler, E. Kirilov, I. Kozyryev, B. R. O'Leary, C. D. Panda, M. F. Parsons, E. S. Petrik, B. Spaun, A. C. Vutha and A. D. West, *Science*, 2014, **343**, 269.

[77] A. Le, M. C. Heaven and T. C. Steimie, *J. Chem. Phys.*, 2014, **140**, 024307.

[78] V. Goncharov and M. C. Heaven, *J. Chem. Phys.*, 2006, **124**, 064312.

[79] C. T. Dewberry, K. C. Etchinson and S. A. Cooke, *Phys. Chem. Chem. Phys.*, 2007, **9**, 4895.

Paweł Tecmer

[80] G. Edvinsson and A. Lagerqvist, *Phys. Scr.*, 1984, **30**, 309.

[81] L. Andrews, M. Zhou, B. Liang, J. Li and B. E. Bursten, *J. Am. Chem. Soc.*, 2000, **122**, 11440.

[82] G. P. Kushto and L. Andrew, *J. Phys. Chem. A*, 1999, **103**, 4836.

[83] W. Küchle, M. Dolg and H. Preuss, *J. Chem. Phys.*, 1994, **100**, 7535.

[84] J. Paulovic, T. Nakajima, K. Hirao, R. Lindh and P. Malmqvist, *J. Chem. Phys.*, 2003, **119**, 798.

[85] A. Kovács and R. J. M. Konings, *J. Phys. Chem. A*, 2011, **115**, 6646.

[86] B. Liang and L. Andrews, *J. Phys. Chem. A*, 2002, **106**, 4038–4509.

[87] J. H. Bartlett, I. O. Antonov and M. C. Heaven, *J. Phys. Chem. A*, 2013, **117**, 12042–12048.

[88] C. C. L. Pereira, C. J. Marsden, J. Marcalo and J. K. Gibson, *Phys. Chem. Chem. Phys.*, 2011, **13**, 12940–12958.

[89] S. Fortier and T. W. Hayton, *Coord. Chem. Rev.*, 2010, **254**, 197–214.

[90] J. Bullock, *J. Chem. Soc. A*, 1969, 781–784.

[91] G. S. Groenewold, A. K. Gianotto, M. E. McIlwain, M. J. van Stipdonk, M. Kullman, D. T. Moore, N. Polfer, J. Oomens, I. Infante, L. Visscher, B. Siboulet and W. A. de Jong, *J. Phys. Chem. A*, 2008, **112**, 508.

[92] G. S. Groenewold, M. J. Van Stipdonk, W. A. de Jong, J. Oomens, G. L. Gresham, M. E. McIlwain, D. Gao, B. Siboulet, L. Visscher, M. Kullman and N. Polfer, *ChemPhysChem*, 2008, **9**, 1278–1285.

[93] G. S. Groenewold, M. J. van Stipdonk, J. Oomens, W. A. de Jong, G. L. Gresham and M. E. McIlwain, *Int. J. Mass spectrom.*, 2010, **297**, 67–75.

[94] V. Vallet, U. Wahlgren and I. Grenthe, *J. Phys. Chem. A*, 2012, **115**, 12373–12380.

[95] L. R. Morss, N. M. Edelstein and J. Fuger, *The Chemistry Of The Actinide And Transactinide Elements*, Springer, Dordrecht, 2010.

[96] J. C. Sullivan, A. J. Zielen and J. C. Hindman, *J. Am. Chem. Soc.*, 1960, **82**, 5288–5292.

[97] J. C. Sullivan, J. C. Hindman and A. J. Zielen, *J. Am. Chem. Soc.*, 1961, **83**, 3373–3378.

[98] C. Madic, B. Guillaume, J. C. Morriseau and J. P. Moulin, *J. Inorg. Nucl. Chem.*, 1979, **41**, 1027–1031.

[99] N. N. Krot and M. S. Grigoriev, *Russ. Chem. Rev.*, 2004, **73**, 89–100.

Paweł Tecmer

[100] R. J. Baker, *Chem. Eur. J.*, 2012, **18**, 16258–16271.

[101] V. N. Serezhkin, G. V. Sidorenko, D. V. Pushkin and L. B. Serezhkina, *Radiochemistry*, 2014, **56**, 115–133.

[102] F. Burdet, J. Pecaut and M. Mazzanti, *J. Am. Chem. Soc.*, 2006, **128**, 16512–16513.

[103] P. Tecmer, N. Govind, K. Kowalski, W. A. de Jong. and L. Visscher, *J. Chem. Phys*, 2013, **139**, 034301.

[104] M. L. McKee and M. Swart, *Inorg. Chem.*, 2005, **44**, 6975–6982.

[105] F. Ruipérez, C. Danilo, F. Réal, J.-P. Flament, V. Vallet and U. Wahlgren, *J. Phys. Chem. A*, 2009, **113**, 1420–1428.

Paweł Tecmer